

SCALAR FIELDS AND LIMBIC MEASUREMENTS OVER THE UNIT DISK *

D. M. TOPA*[†], P. F. EMBID*, AND J. H. COOLEY*

Abstract. The goals of this paper are to present basic mathematical tools for the analysis of scalar fields over the unit disk. In particular, we discuss limbic measurements in the continuum limit and for spatially extended sources and detectors. The physical motivation is x-ray spectroscopy of spheres under radiative compression and as such this work covers mathematical preliminaries for a 2-D approximation in advance of a complete 3-D analysis.

Key words. Radiative transport, Zernike polynomials, limbic measurement

AMS subject classifications. 15-02, 33E-02

1. Introduction. Our physical motivation is to study radiative implosion of spherical capsules of isotopic hydrogen. Such experiments are the staple at facilities like the National Ignition Facility and the Omega Laser Facility. Typical capsules are tiny with a radius of one to two millimeters. They are pressurized at 10 to 15 atmospheres. They may be cryogenically cooled or at room temperature. They often contain a mix of deuterium, D, and tritium, T.

To help focus the analysis, we assume the capsules are compressed uniformly by a bath of high energy x-rays. We assume the outer shell of the capsule is ablated creating an inward compression due to the rocket effect [?]. We are interested in cases where the capsule shell is sturdy enough to support uniform compression; that is, the capsule boundary remains spherical until maximum compression is reached (bang time). One valuable diagnostic is a dopant which produces a bright x-ray source in the temperature and pressure ranges of interest. For example, this may be a smattering of argon gas inside the capsule or titanium dopant in the outer shell. The measurement of interest is the intensities for the two dominant x-ray lines.

The detectors which record these intensities resolve the capsule into 5–25 radial zones. There are detectors on three spatial axes to allow three-dimensional imaging of the capsule. While our ultimate goal is to study phenomena like the Rayleigh-Taylor instability which shatter spherical symmetries, we are interested in developing foundation tools which use intensity measurements to divine thermodynamic profiles inside the capsule. This motivates an initial consideration of spherical symmetry.

[†]Los Alamos National Laboratory, Los Alamos New Mexico 87545

²Department of Mathematics and Statistics, University of New Mexico, Albuquerque New Mexico 87131

*This work was supported by the Society for Industrial and Applied Mathematics

2. Radiative transport. For the problem at hand the data is a spatially resolved set of x -ray intensity measurements. A dopant in the device is selected to create a known signature over a temperature and pressure regime of interest. We rely upon this signature to resolve the thermodynamic profiles in the capsule. The mathematical challenge before us is to use the intensity measurements and the radiative transport equation to divine the physics inside the capsule.

Consider a photon packet within the capsule. Between creation and detection we will consider three mathematically distinct phenomena: absorption, emission and scattering.

We treat the radiative transport equation as a one-dimensional integro-differential equation of the form $Lu(r, \mu) = f(r)$

$$(2.1) \quad \left(\mu \frac{\partial}{\partial r} + \frac{1 - \mu^2}{r} \frac{\partial}{\partial \mu} + k(r) \right) I(r, \mu) + \frac{1}{4\pi} \int_{4\pi} \mu_s(r, \omega \cdot \hat{\omega}) I_\nu(s, \omega) d\hat{\omega} = -k(r) J(r)$$

For comparison, see Hummer[2].

The archetype ODE for radiative transport is

$$(2.2) \quad I'(s) + I(s) = 1$$

which is a decay equations with a forcing term.

$$(2.3) \quad I(r) = e^{-\int_r^1 \alpha(r') dr'} \left(1 - \int_r^1 e^{\int_{r'}^1 \alpha(r'') dr''} j(r'') dr' \right)$$

2.1. Closing. In our application we enjoy the benefit of having functional forms for the absorption $\alpha(T, \rho)$ and emission $j(T, \rho)$.

The long range goal is to find 3D solutions of the form $\psi(r, \theta, \phi)$ using a scattering kernel. But there are mathematical preliminaries to address.

In this treatment we avoid the necessary evil of units for two reasons. First, the measurement is

The mathematical problem distills to this: given an intensity profile $\psi(r)$ and the maps $\alpha(T, \rho)$ and $j(T, \rho)$ find the thermodynamic profile $T(r)$ and $\rho(r)$ inside the capsule assuming the validity of the radiative transport equation.

1. Compute opacity map $\alpha(T, \rho)$ and emissivity map $j(T, \rho)$.
2. Use detector measurements to find the integrated intensity $\mathcal{I}(r)$.
3. Construct $\alpha(r)$ and $j(r)$.
4. Compute thermodynamic profiles $T(r)$ and $\rho(r)$.

3. Polynomial basis. Of interest are spherically symmetric functions $\psi: \mathbb{R}^2 \mapsto \mathbb{R}$. We require functions square-integrable over the unit disk $L_2(\overline{D}_2)$. The two most common polynomial sets are the one posed by Zernike [6] and the other proposed by Bhatia and Wolf [1]. Both sets are discussed briefly in the appendix. For either case, we are interested in a rotationally invariant subset where the angular frequency $m = 0$.

3.1. Polynomial basis. We choose the set of Zernike because of the order-by-order correspondence to the Seidel aberrations and we adopt Zernike's convention

$$(3.1) \quad V_n^m(r, \theta) = R_n^m(r) e^{im\theta}$$

where n and m are positive integers such that $n - m$ is a positive, even number. The order is n , the angular frequency is m . The radial functions are defined in the appendix. The full set

$$\{V_0^0(r, \theta), V_1^1(r, \theta), V_2^0(r, \theta), V_2^2(r, \theta), \dots\}$$

is complete[?] over the unit disk and this allows for the uniform approximation of continuous.

$$(3.2) \quad \psi(r, \theta) = \sum_{n=0}^d \sum_{m=\odot}^{n(2)} \alpha_{n,m} R_n^m(r) e^{im\theta}, \quad \alpha \in \mathbb{C}^{\frac{1}{2}d(d+1)}$$

The degree of the fit is $d = 0, 1, 2, \dots$. The sum over m runs from $\odot = n \bmod 2$ to n in increments of 2. For example, when the order $n = 4$ the angular velocity takes the values $m = 0, 2, 4$; for $n = 5$ we have $m = 1, 3, 5$.

Eventually we need to consider fields like $\psi(r, \theta)$ with angular dependence. The first stage of this analysis is restricted to radially symmetric fields $\psi(r)$ which restricts us to the subset of the Zernike polynomials with radial symmetry. This is set with angular frequency $m = 0$.

One must establish that the completeness of the culled set with $m = 0$ is dense in the space of continuous, rotationally invariant functions with respect to the uniform norm. This task is simplified by Trent's extension [3] of the Müntz-Szász theorem to the closed unit disk. Consider the space $L_2(\overline{D}_2)$ and let S be the span of the set of monomials of even powers $\{1, r^2, r^4, \dots\}$.¹ The closure of S is the set \overline{S} which represents the rotationally invariant elements which can be approximated by polynomials. In this case $\overline{S} \subseteq L_2(\overline{D}_2)$. The following theorem connects the reduced Zernike polynomials and the even monomials.

THEOREM 3.1 (Completeness). *The Zernike polynomial set with angular frequency $m = 0$ is dense in the space of rotationally invariant functions in \overline{D}_2 with respect to the uniform norm.*

Proof. From (A.2) the recursion relationship for this reduced set is

$$(3.3) \quad R_{2k}^0(r) = \sum_{j=0}^k (-1)^j \frac{(2k-j)!}{j!((k-j)!)^2} r^{2(k-j)}, \quad k = 0, 1, 2, \dots$$

The coefficients are positive and never 0 which implies that the polynomial of order n is a function of the form

$$R_n^0(r) = a_0 + a_2 r^2 + \dots + a_n r^n$$

where $a_{2k} > 0$, $k = 0, 1, 2, \dots, n$. From this we have an equivalence between the span S of the Zernike set and S' of the even monomials:

$$\text{sp} \{R_{2k}^0(r)\}_{k=0}^n = \text{sp} \{r^{2k}\}_{k=0}^n.$$

This relationship holds in the limit $n \rightarrow \infty$. Therefore the Zernike polynomial set with angular frequency $m = 0$ is spanned by the set of even polynomials in r . The sum of the inverse of these monomial powers diverges

$$\lim_{n \rightarrow \infty} \sum_{k=1}^n \frac{1}{2k} \rightarrow \infty.$$

¹We define $\lim_{r \rightarrow 0} r^0 \equiv 0$.

By the Müntz-Szász theorem for \overline{D}_2 , the closed span $\overline{S'}$ is dense in $L^2(\overline{D}_2)$, and hence by equivalence so is \overline{S} . \square

The reduced polynomial set for $m = 0$ is previewed in figure (1) as two subsets, a presentation which reminds us that the individual sequences for k even and k odd are Cauchy. These two sequences are further distinguished by their behavior at $r = 1/\sqrt{2}$. Given $k = 0, 1, 2, \dots$,

$$(3.4) \quad \begin{aligned} R_{2(2k)}^0 \left(1/\sqrt{2} \right) &= 0, \\ \frac{d}{dr} R_{2(2k+1)}^0 \left(1/\sqrt{2} \right) &= 0. \end{aligned}$$

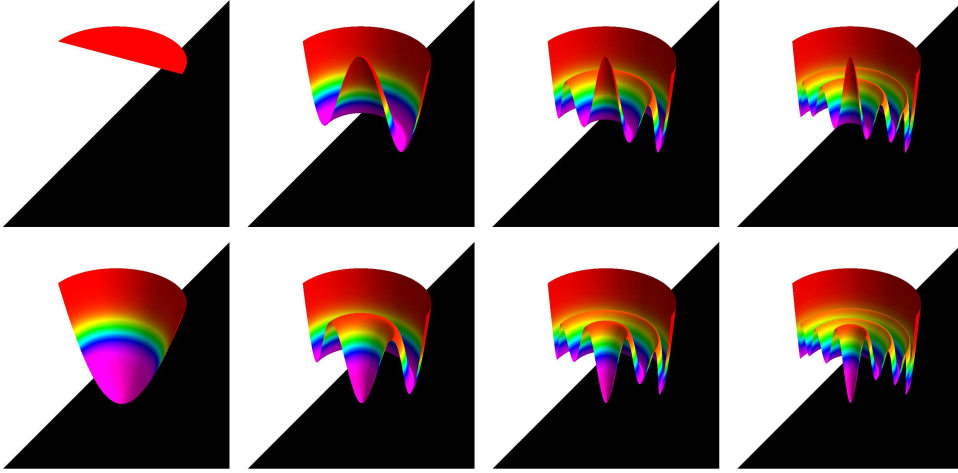


FIG. 1. Function sequences for the angular velocity $m = 0$ subset grouped by parity and shown in cutaway: $\{Z_{2(2k)}^0(r, \theta)\}_{k=0}^3$ (top), and $\{Z_{2(2k+1)}^0(r, \theta)\}_{k=0}^3$ (bottom). The Fourier like nature of these polynomials is apparent; the top row functions like cosine terms, the bottom like sine terms.

These polynomials are used to represent rotationally invariant scalar fields over the unit disk. Let n be the highest order term in the sequence, the expansion is cast with amplitudes α :

$$(3.5) \quad \psi(r) = \alpha_0 + \alpha_2 R_2^0(r) + \alpha_4 R_4^0(r) + \dots + \alpha_n R_n^0(r) = \sum_{k=0}^d \alpha_{2k} R_{2k}^0(r)$$

The summation control parameter $d = n/2$. The scalar field $\psi(r)$ represents measurable scalars such as intensity, temperature or density. The orthogonality of the Zernike polynomial set is a useful property (as seen in the following theorem (3.1) and [5]). Yet the linear independence of this set is most often the property to exploit as in theorem (3.1). The reason for this is two fold.

First, Zernike's polynomials are constructed to be in an order-by-order correspondence with the optical aberrations popularized by Seidel [6]. This empowers exact affine transformations between the representations of Zernike and Seidel. Secondly, orthogonality is predicated upon the domain and the topology. The Zernike polynomials are orthogonal over $L^2(\overline{D}_2)$ but not upon $l^2(\overline{D}_2)$. Since measurements are inherently finite objects and computer algorithms are built upon discrete meshes we

are excluded from using orthogonality² and rely instead upon linear independence. We are thus compelled to built our approximation upon the minimal spanning set, the monomials:

$$(3.6) \quad \psi(r) = a_0 + a_2 r^2 + a_4 r^4 + \cdots + a_n r^n = \sum_{k=0}^d a_{2k} r^{2k}$$

A simple change of basis toggles the coordinates α in the Zernike basis and the coordinates a in the monomial basis:

$$(3.7) \quad \alpha = [T]_{Zernike}^{-1} a.$$

The three lowest Zernike polynomials have the monomial representation $R_0^0(r) = 0$, $R_0^0(r) = 2r^2 - 1$ and $R_6^0(r) = 6r^4 - 6r^2 + 1$, the change of basis matrix is

$$(3.8) \quad [T]_{Zernike}^{-1} = \begin{bmatrix} 1 & -1 & 1 \\ 0 & 2 & -6 \\ 0 & 0 & 6 \end{bmatrix}^{-1}$$

Very much like a Fourier decomposition, the Zernike composition describes zero mean oscillations about a constant value given by the order $n = 0$ amplitude. This is not apparent given the polynomial weighting in the Zernike terms seen in (3.1). However, the following proof verifies the contention. (The proof is trivially extended to include $m = 1, 2, \dots$)

THEOREM 1 (Mean value for Zernike expansions). *Given the Zernike polynomial expansion over \overline{D}_2 in (3.2) the mean value of the function $\psi(r, \theta)$ is given by*

$$(3.9) \quad \langle \psi(r, \theta) \rangle_{\overline{D}_2} = \alpha_{0,0}.$$

Proof. Define the mean value of the function as

$$(3.10) \quad \langle \psi(r, \theta) \rangle_{\overline{D}_2} = \frac{\int_{\overline{D}_2} \psi(r, \theta) r dr d\theta}{\int_{\overline{D}_2} r dr d\theta}.$$

Since the radial polynomials and exponential terms are continuous functions on a compact interval we may safely interchange the order of summation and integration:

$$(3.11) \quad \int_{\overline{D}_2} \psi(r, \theta) r dr d\theta = \sum_{n=0}^d \sum_{m=\odot}^{n(2)} \alpha_{n,m} \int_0^1 R_n^m(r) \int_0^{2\pi} e^{im\theta} d\theta r dr$$

where we allow the limit $d \rightarrow \infty$.

This proof resolves two different regimes for the angular velocity $m \in \mathbb{N}$: the first $m > 0$, the second $m = 0$. This distinction arises from the integration of the angular variable:

$$(3.12) \quad \int_0^{2\pi} e^{im\theta} d\theta = \begin{cases} 0 & m \neq 0 \\ 2\pi & m = 0 \end{cases}.$$

²Codes built upon orthogonality extend computation time; for a mesh of N points the error in the accuracy is $\mathcal{O}(N)$. Zernike expansion amplitudes are no longer independent and cannot be calculate linearly. This demands the solution of a full rank linear system [4].

The expansion terms corresponding to values of $m > 0$ do not contribute to mean value. We now address the rotationally invariant terms where $m = 0$ and here too we find a distinction this time for $k = 0$ and $k \geq 1$. The assertion in (3.9) is now restated for $k \in \mathbb{N}$ as

$$(3.13) \quad \int_0^1 R_{2k}^0(r) r dr = \begin{cases} \frac{1}{2} & k = 0 \\ 0 & k \geq 1 \end{cases}$$

The case of $k = 0$ is trivial and we must exhibit the veracity of the claim for $k \geq 1$. Integrate the terms in (A.2).

$$(3.14) \quad \frac{(2k-j)!}{j!((k-j)!)^2} \int_0^1 r^{2(k-j)} r dr = \frac{1}{2(k-j+1)} \frac{(2k-j)!}{j!((k-j)!)^2}$$

The integral for each polynomial of order $2k$ is reduced to the sum

$$(3.15) \quad \mathcal{S}_k = \int_0^1 R_{2k}^0(r) r dr = \sum_{j=0}^k \frac{(-1)^j}{2(k-j+1)} \frac{(2k-j)!}{j!((k-j)!)^2}$$

and we employ induction to prove $\mathcal{S}_k = 0$ for $k \geq 1$. The base case is $\mathcal{S}_1 = \frac{1}{2} - \frac{1}{2} = 0$. For $k > 1$ we assume $\mathcal{S}_k = 0$ and exploit this to establish $\mathcal{S}_{k+1} = 0$. The proof strategy is to demonstrate that $\mathcal{S}_k + \mathcal{S}_{k+1} = 0$.

The sum of consecutive sequences is

$$(3.16) \quad \mathcal{S}_k + \mathcal{S}_{k+1} = \frac{1}{2(k+2)} \frac{(2k+2)!}{((k+1)!)^2} + \sum_{j=0}^k (-1)^j \left(1 - \frac{2(k-j)}{j+1}\right) \frac{(2k-j)!}{j!((k-j)!)^2} = 0$$

which implies, after simplification of the summation terms, that

$$(3.17) \quad \frac{1}{2(k+2)} \frac{(2k+2)!}{((k+1)!)^2} = - \sum_{j=0}^k (-1)^j \frac{(k-j)(k-j+1)(2k-j)!}{(j+1)!((k-j)!)^2}.$$

The sum in (3.17) can be evaluated:

$$(3.18) \quad \sum_{j=0}^k (-1)^j \frac{(k-j)(k-j+1)(2k-j)!}{(j+1)!((k-j)!)^2} = -\frac{k+1}{k+2} \frac{(2k+1)!}{((k+1)!)^2}.$$

With modest manipulation we connect to (3.16):

$$(3.19) \quad \frac{k+1}{k+2} \frac{(2k+1)!}{((k+1)!)^2} = \frac{1}{2(k+2)} \frac{(2k+2)!}{((k+1)!)^2}.$$

This substantiates $\mathcal{S}_k + \mathcal{S}_{k+1} = 0$, therefore $\mathcal{S}_{k+1} = 0$. Therefore (3.15) is valid, therefore

$$(3.20) \quad \int_0^1 R_{2k}^0(r) r dr = 0, \quad k \geq 1.$$

This establishes

$$(3.21) \quad \sum_{k=0}^{\infty} \left(\alpha_{2k,0} \int_0^1 R_{2k}^0(r) r dr \right) = \frac{1}{2} \alpha_{00}$$

which confirms the contention in (3.9). \square

The immediate advantage is that the Zernike decompositions automatically provide for mean values including valuable thermodynamic properties such as temperature and pressure.

3.2. Trajectories. With the scalar fields being represented by a Zernike expansion, These are generalized Lissajous figures.

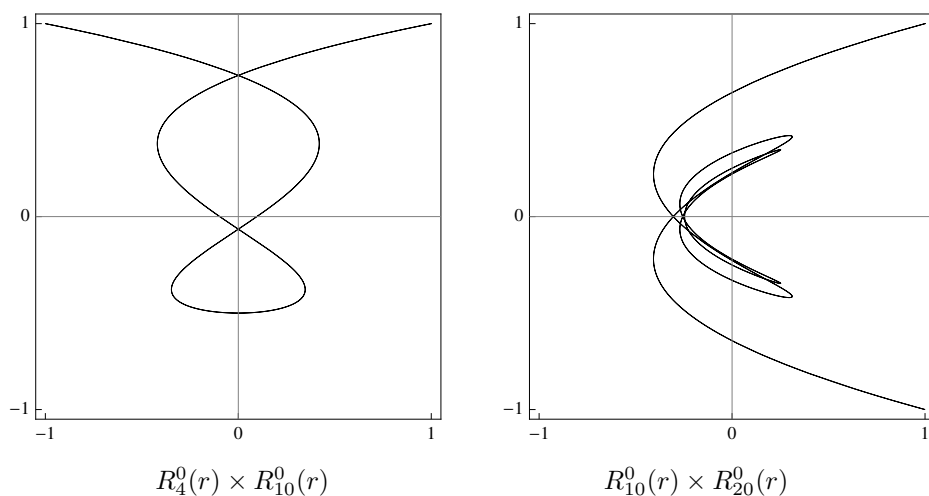


FIG. 2. Generalized Lissajous figures using the ideal gas law (??) for the equation of state.

4. Limbic measurement. In experimental measurements of interest (such as those at NIF and the Omega Laser Facility) the detector array is in the plane of the unit disk and views a portion of the disk over the range $-\pi/2 \leq \phi \leq \pi/2$. The angle is defined on the disk and the ray at $\phi = 0$ intersects the detector array at a right angle. What the detectors record in the x -ray intensity integrated along a limbic path. We now discuss the geometry of these paths.

4.1. Infinitesimal detectors (Continuum case). We start with the idealization of infinitesimal detectors. Basic detector geometry is shown in figure (3) where the detector plane represents a continuum of detectors. These detectors record a response function $Y(b)$ where b is the impact parameter, an offset from the ray at $\phi = 0$. Handling this offset requires some attention.

While we are trying to discern $\psi(r)$ a scalar field as a function of distance from the origin, we record the integral of an intensity function along the limbic paths in figure (3). Let γ_b represent one such path as seen in figure (4). The detector at b measures the intensity at the surface of the capsule; the measurement is the response function $Y(b)$.

4.1.1. Response function. The response function is an integral along the limbic path characterized by an impact parameter b :

$$(4.1) \quad Y(b) = \int_{\gamma_b} \psi(s) ds.$$

The measurement represents the strength of the photon packet exiting the capsule. These photons encode thermodynamic information along the the path γ_b . This path

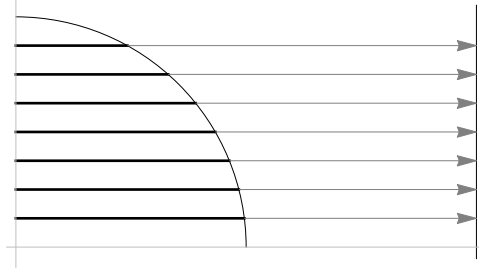


FIG. 3. *Basic detector geometry. The quarter capsule is shown on the left, the detectors as a plane on the right. The dark lines represent packets of x-rays traveling through and interacting with the capsule. Because of an imaging system, the detectors see the intensity at the surface of the capsule which is transported to the detectors. The line of site is characterized by an impact parameter b measuring distance from the equator. Our discussion first considers the case where b is a continuous variable $0 \leq b \leq 1$, from the equator to the apex.*

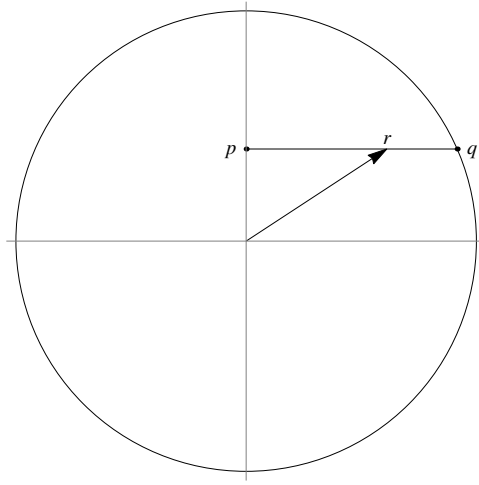


FIG. 4. *The line integral in figure (3). The path γ_b is the convex set connecting p to q . The magnitude of the vector r is given as a function of the parameter b .*

is the convex set connecting $p = \begin{bmatrix} b \\ 0 \end{bmatrix}$ to $q = \begin{bmatrix} b \\ \sqrt{1-b^2} \end{bmatrix}$:

$$(4.2) \quad \gamma_b(t) = p(1-t) + qt, \quad 0 \leq t \leq 1.$$

This formulation establishes convexity.

To parameterize the function ψ along this line given by $0 \leq x_1 \leq \sqrt{1-b^2}$, $x_2 = b$ define the radial distance r in figure (4) as

$$(4.3) \quad r = \sqrt{x_1^2 + b^2}$$

then the integral in (4.1) becomes

$$(4.4) \quad \begin{aligned} Y(b) &= \int_0^{\sqrt{1-b^2}} \psi \left(\sqrt{x_1^2 + b^2} \right) dx_1, \quad b \in [0, 1] \\ &= \int_0^{\sqrt{1-b^2}} \left(a_0 \left(\sqrt{x_1^2 + b^2} \right)^0 + a_2 \left(\sqrt{x_1^2 + b^2} \right)^2 + a_4 \left(\sqrt{x_1^2 + b^2} \right)^4 + \dots \right) dx_1 \end{aligned}$$

For $k = 0, 1, 2, \dots$ the integrals in (4.4) is

$$(4.5) \quad \int_0^{\sqrt{1-b^2}} \left(\sqrt{x_1^2 + b^2} \right)^{2k} dx_1 = \left(2b^2 \sqrt{1-b^2} (k+1) \right)^{-1} \times \\ \left({}_2F_1 \left(1, k + \frac{3}{2}; -\frac{1}{2}; 1 - \frac{1}{b^2} \right) + (2b^2(k+2) - 2k - 5) {}_2F_1 \left(1, k + \frac{3}{2}; \frac{1}{2}; 1 - \frac{1}{b^2} \right) \right).$$

For $|z| > 1$ and $a - b \notin \mathbb{Z}$ the hypergeometric series is defined³ as

$$(4.6) \quad {}_2F_1(a, b; c; z) = \frac{\Gamma(b-a)\Gamma(c)(-r)^{-a}}{\Gamma(b)\Gamma(c-a)} \sum_{k=0}^{\infty} \frac{(a)_k(a-c+1)_k z^{-k}}{k!(a-b+1)_k} \\ + \frac{\Gamma(a-b)\Gamma(c)(-r)^{-b}}{\Gamma(a)\Gamma(c-b)} \sum_{k=0}^{\infty} \frac{(b)_k(b-c+1)_k z^{-k}}{k!(a-b+1)_k}$$

and the rising Pochhammer symbol is

$$(4.7) \quad (a)_n = \begin{cases} 1 & n = 0 \\ a(a+1) \dots (a+n-1) & n > 0 \end{cases}$$

For this problem the arguments of the Pochhammer function are natural numbers and we may use this definition:⁴

$$(4.8) \quad (a)_n = \frac{\Gamma(a+n)}{\Gamma(a)}.$$

Equation (4.6) tames the unbounded growth of the $1/b^2$ term in the function argument.

The modes in the expansion (3.6) imprint upon (4.4) motivating the need to resolve the response function⁵ into modes:

$$(4.9) \quad \begin{aligned} \mathcal{Y}_0(b) &= \int_0^{\sqrt{1-b^2}} \left(\sqrt{x_1^2 + b^2} \right)^0 dx_1 = \sqrt{1-b^2} \\ \mathcal{Y}_2(b) &= \int_0^{\sqrt{1-b^2}} \left(\sqrt{x_1^2 + b^2} \right)^2 dx_1 = \frac{1}{3} (1 + 2b^2) \sqrt{1-b^2} \\ \mathcal{Y}_4(b) &= \int_0^{\sqrt{1-b^2}} \left(\sqrt{x_1^2 + b^2} \right)^4 dx_1 = \frac{1}{15} (3 + 4b^2 + 8b^4) \sqrt{1-b^2} \\ &\vdots \end{aligned}$$

³Wolfram Functions Site, <http://functions.wolfram.com/HypergeometricFunctions/Hypergeometric2F1/02/02/>.

⁴NIST Digital Library of Mathematical Functions, <http://dlmf.nist.gov/5.2>.

⁵To avoid the ambiguous form 0^0 , we define the iterated limit in the response function as $\lim_{r \rightarrow 0, n \rightarrow 0} r^n \equiv 1$.

The approximation in (4.4) takes the form

$$(4.10) \quad Y(b) \approx a_0 \mathcal{Y}_0(b) + a_2 \mathcal{Y}_2(b) + a_4 \mathcal{Y}_4(b) + \dots$$

The response functions \mathcal{Y} can be assembled using recursion as seen the in following lemma.

THEOREM 2 (Recursion). *The integrals in (4.9) can be generated using*

$$(4.11) \quad \begin{aligned} \mathcal{Y}_0(b) &= \sqrt{1-b^2} \\ \mathcal{Y}_{n+2}(b) &= \left((n+2) \frac{b^2}{\sqrt{1-b^2}} \mathcal{Y}_n(b) + 1 \right) \frac{\sqrt{1-b^2}}{n+3}, \quad n = 2, 4, 6, \dots \end{aligned}$$

Proof. The base case $\mathcal{Y}_0(b)$ is trivial; consider $n = 2, 4, \dots$. Attack the integral

$$(4.12) \quad \mathcal{Y}_n(b) = \int_0^{\sqrt{1-b^2}} \left(\sqrt{x_1^2 + b^2} \right)^n dx_1$$

using integration by parts, $\int u dv = uv - \int v du$, where

$$(4.13) \quad u = \left(\sqrt{x_1^2 + b^2} \right)^n, \quad dv = dx_1$$

which leads to the identity

$$(4.14) \quad \int_0^{\sqrt{1-b^2}} \left(\sqrt{x_1^2 + b^2} \right)^n dx_1 = \sqrt{1-b^2} - n \int_0^{\sqrt{1-b^2}} x_1^2 \left(\sqrt{x_1^2 + b^2} \right)^{n-2} dx_1.$$

Let the multiplicative factor $x_1^2 = x_1^2 + b^2 - b^2$ and shift the index n up by 2 to recover (4.11). \square

The polynomial portion of the sequence \mathcal{Y}

$$(4.15) \quad \left\{ 1, \frac{1}{3} (1 + 2b^2), \frac{1}{15} (3 + 4b^2 + 8b^2), \frac{1}{35} (5 + 6b^2 + 8b^4 + 16b^6, \dots) \right\}$$

is a series of bowl functions as seen in figure 5. This figure suggests that we can expect problems resolving data near the apex of the capsule where $b = 1$.

The lowest modes \mathcal{Y} are displayed in figure (6), a plot which inspires the following proof.

THEOREM 3 (Majorization of the sequence of response functions). *Given the function sequence in (4.9), the functions are majorized according to*

$$(4.16) \quad \mathcal{Y}_{n+2}(b) \geq \mathcal{Y}_n(b), \quad n = 0, 1, 2, \dots$$

Proof. Define $\rho = \sqrt{x_1^2 + b^2}$. Given $b \in [0, 1]$, we have $0 \leq \rho \leq \sqrt{1-b^2} \leq 1$ accordingly $\rho^2 \leq 1$. Therefore

$$(4.17) \quad \int_0^{\sqrt{1-b^2}} \rho^2 \rho dx_1 \leq \int_0^{\sqrt{1-b^2}} \rho dx_1,$$

with the equality is achieved in the limit $b \rightarrow 1$. \square

For example if the amplitudes in the ψ expansion in (3.6) are ordered

$$a_0 \geq a_1 \geq \dots \geq a_n,$$

then the coefficients in the $Y(b)$ expansion in (4.10) are also ordered.

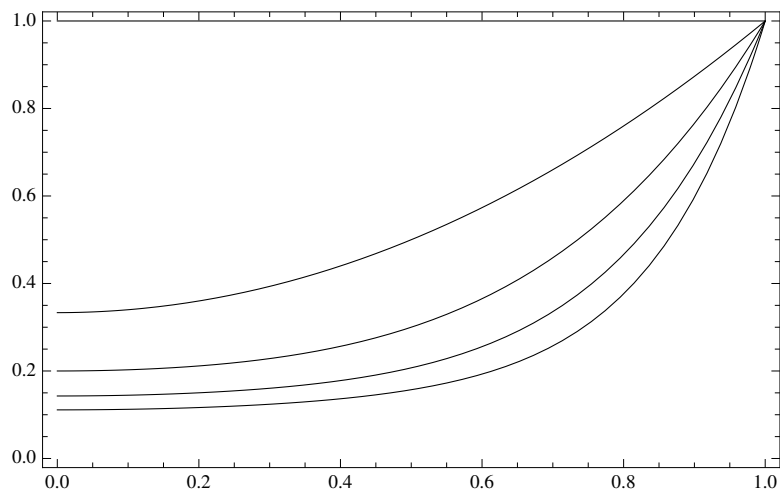
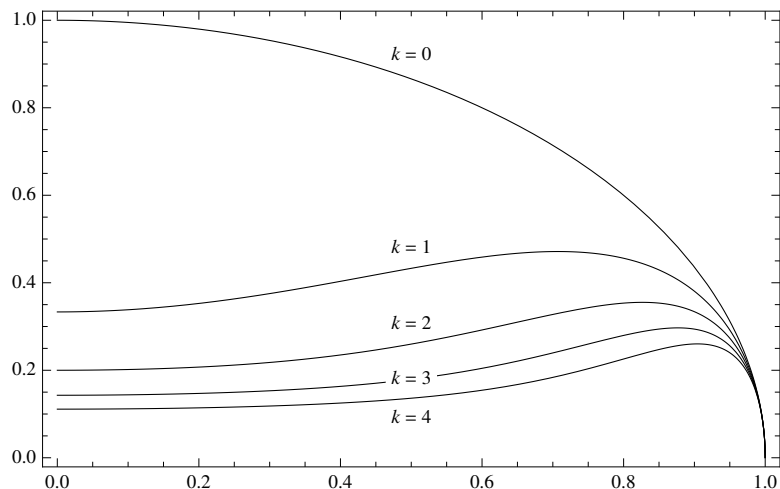


FIG. 5. The sequence of bowl functions in (4.15).

FIG. 6. The family of curves in (4.9) for $k = 0, 1, 2, 3, 4$. For low to medium impact parameters b we see a dominance by the lowest order modes.

4.1.2. Example: Top hat. For clarity, consider the example of an intensity function described as a top hat function:

$$(4.18) \quad \psi(r) = \begin{cases} 1 & r \leq \frac{1}{2} \\ 0 & r > \frac{1}{2} \end{cases}.$$

Physically this function describes a capsule with two zones. The inner zone has a uniform brightness and the outer is dark and nonabsorbent. It allows the light from the inner zone to pass through without change. While this is a simple physical concept, this C^0 function presents a challenge in polynomial decomposition.

Figure 1 shows the resolution of the top hat function into two bases: the even monomials and the Zernike radial polynomials. Since we are dealing with a C^0 function we lose the uniform convergence of the Weierstrass theorem and fall back to

pointwise convergence. The maximum order of fit is shown in the first column. The next column displays the polynomial reconstruction against the top hat with the Gibbs phenomena prominent at the discontinuity and at the boundary points. The next two columns plot the amplitudes in the Zernike (α_{2k}) and the monomial (a_{2k}) basis on a logarithmic scale. Amplitudes with positive values are plotted in black. Negative amplitudes are plotted by absolute value and represented by the red points. An exact affine transformation relates the α and a sets. A compelling reason to use the Zernike basis is to avoid the unbounded growth evident in the monomial set. Another distinction is computing time. The Zernike amplitudes are computed mode-by-mode, whereas the monomial amplitudes demand the solution of a large linear system which is famously ill conditioned.

The response is the C^1 function

$$(4.19) \quad Y(b) = \begin{cases} \sqrt{\frac{1}{4} - b^2} & r \leq \frac{1}{2} \\ 0 & r > \frac{1}{2} \end{cases}$$

The input profile and output response function are shown in table (2).

4.1.3. Inverse problem. Given a response function, a measurement, we need to find input function. To represent the sequence in (4.9), nominate a trial function

$$(4.20) \quad \Upsilon(b) = c_0 \sqrt{1 - b^2} + c_2 \sqrt{1 - b^2} b^2 + c_4 \sqrt{1 - b^2} b^4 + \dots + c_n \sqrt{1 - b^2} b^n$$

where the number of amplitudes is $m = n/2 + 1$. We seek the least squares solution defined as finding the amplitude vector c in the set which minimizes the square of the residual error $\epsilon(b)$:

$$(4.21) \quad \mathcal{C} = \left\{ c \in \mathbb{R}^m : \epsilon(b) = \int_0^1 \|Y(b) - \Upsilon(b)\|_2^2 db \text{ is minimized} \right\}$$

This generates a linear system with normal equations given by

$$(4.22) \quad \mathbf{A}c = y$$

The symmetric matrix $\mathbf{A} \in \mathbb{R}^{m \times m}$ has elements

$$(4.23) \quad A_{rc} = \int_0^1 (1 - b^2) b^{2(r-1)+2(c-1)} db = \frac{2}{(2(r+c)-1)(2(r+c)-3)};$$

and the data vector $y \in \mathbb{R}^m$

$$(4.24) \quad y_r = \int_0^1 Y(b) b^{2(r-1)} db.$$

This produces an amplitude vector c in the Υ basis which is related to the amplitude vector a in the Y basis by a change of basis transformation:

$$(4.25) \quad a = [T]_{\mathbf{y}}^{-1} c.$$

For a sixth order fit like (4.9) the transformation from the c vector in the Υ basis to the a vector in the ψ basis looks like this:

$$(4.26) \quad [T]_{\mathbf{y}}^{-1} = \begin{bmatrix} 1 & 1/3 & 1/5 & 1/7 \\ 0 & 2/3 & 4/15 & 6/35 \\ 0 & 0 & 8/15 & 8/35 \\ 0 & 0 & 0 & 16/35 \end{bmatrix}^{-1},$$

TABLE 1
Resolving the top hat function in two different polynomial bases.

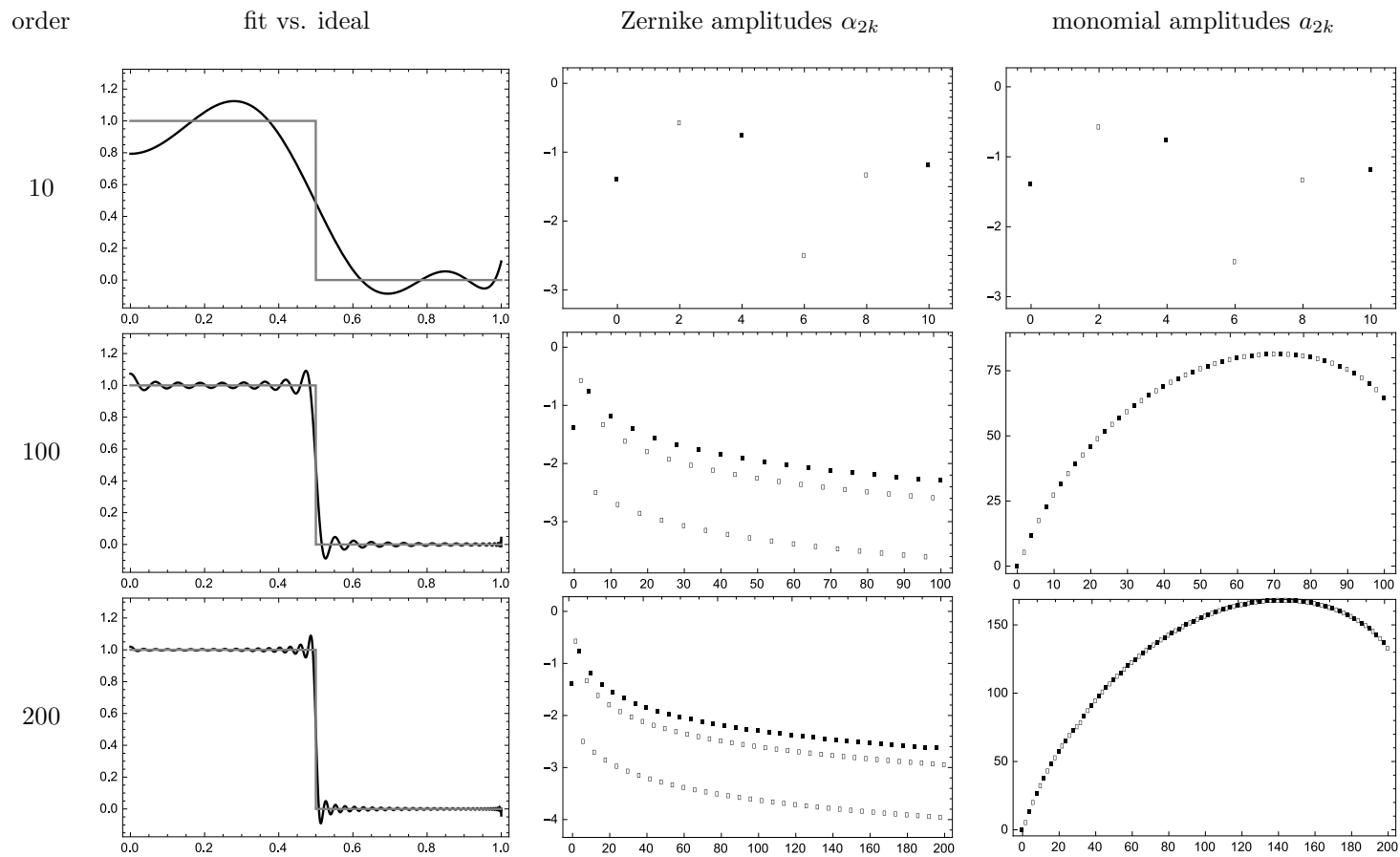
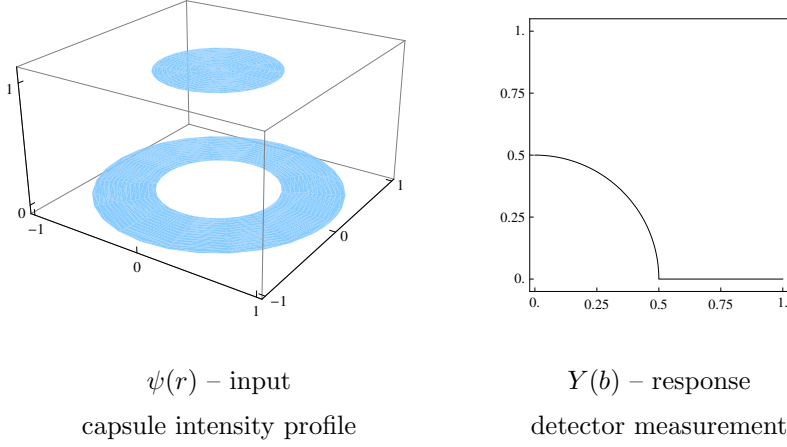


TABLE 2
The top hat function in (4.18) and the response function given in (4.19).



a form which manifestly displays the coordinates in (4.15). To go from the monomial basis a vector to the Zernike basis α vector use the affine transform $\alpha = [T]_Z^{-1} a$ shown here:

$$(4.27) \quad [T]_Z^{-1} = \begin{bmatrix} 1 & -1 & 1 & -1 \\ 0 & 2 & -6 & 12 \\ 0 & 0 & 6 & -30 \\ 0 & 0 & 0 & 20 \end{bmatrix}^{-1},$$

a form which manifestly displays the coordinates in polar coordinates for the $m = 0$ terms in table 6.

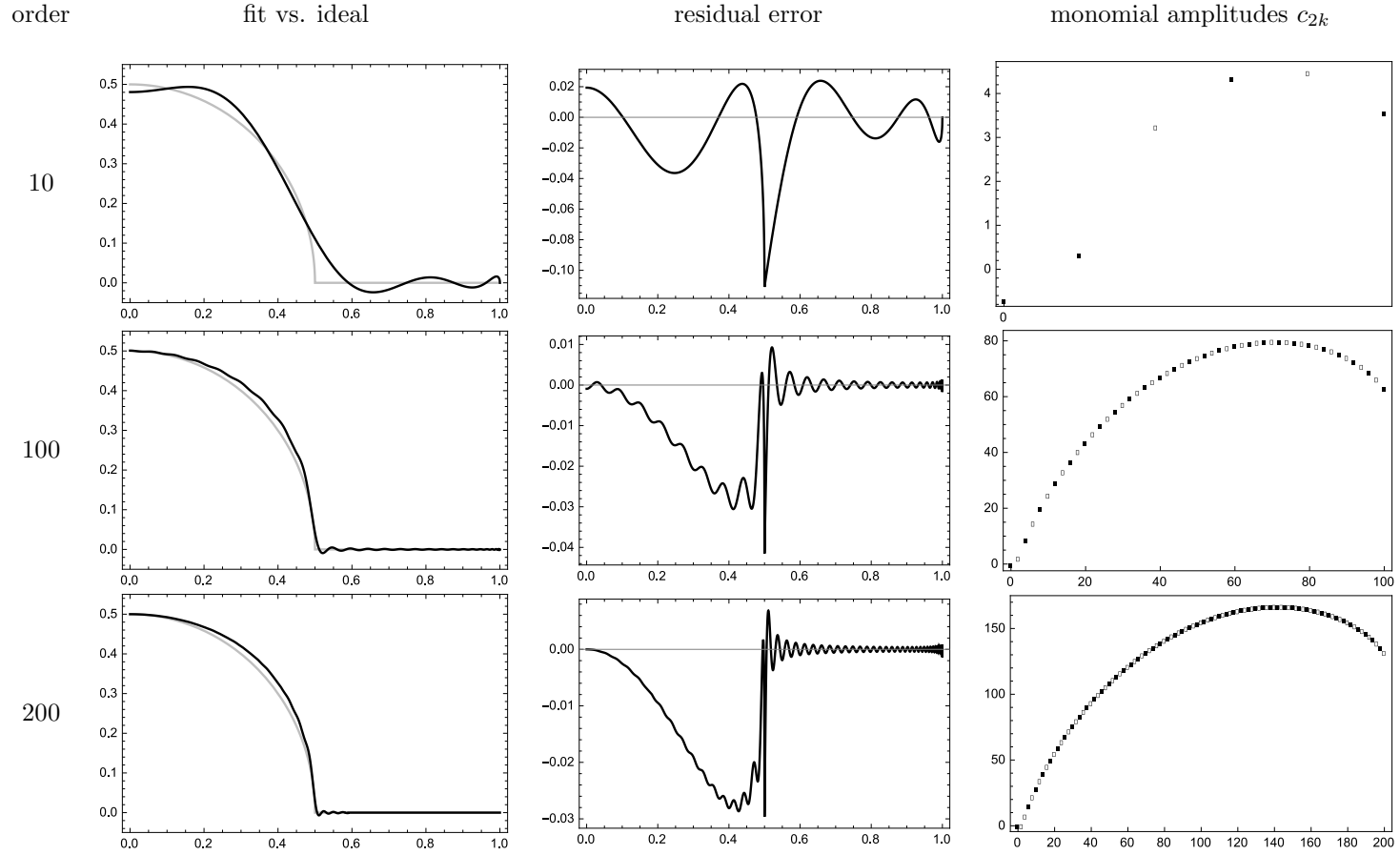
4.1.4. Inverse problem example: top hat. This section shows the results for fits of two different degrees. Results are shown in table (3). Using the response function in (4.19), a data vector was constructed according to (4.24) as was a system matrix using (4.23). This generates the linear system in (4.22) which is solved using least squares to produce the amplitude vector c in (4.20). An affine transformation like the one in equation (??) is used to find the amplitude vector a in (3.6) which resolves the scalar field ψ . A final affine transformation (4.27) recovers the Zernike basis amplitudes α . Schematically,

$$(4.28) \quad \alpha = [T]_Z^{-1} [T]_Y^{-1} c$$

For validation, we provide solutions for the $n = 6$ case. The measurement values here represent the amplitudes of the expansion Υ

$$(4.29) \quad \begin{bmatrix} c_0 \\ c_2 \\ c_4 \\ c_6 \end{bmatrix} = \frac{\pi}{536\,870\,912} \begin{bmatrix} 92\,303\,820 \\ -304\,601\,220 \\ 182\,522\,340 \\ 69\,369\,300 \end{bmatrix}.$$

TABLE 3
Building up the response function $Y(b)$: the amplitudes c in equation (4.20).



Next these coordinates are transformed via $a = [T]_Y^{-1} c$ into the Y basis, which fortuitously, are the same coordinates for the monomial expansion for $\psi(r)$. The final transformation $\alpha = [T]_Z^{-1} a$ is to move from the monomial basis to the Zernike basis:

$$\begin{aligned} \begin{bmatrix} \alpha_0 \\ \alpha_2 \\ \alpha_4 \\ \alpha_6 \end{bmatrix} &= \frac{\pi}{536\,870\,912} \begin{bmatrix} 1 & -1 & 1 & -1 \\ 0 & 2 & -6 & 12 \\ 0 & 0 & 6 & -30 \\ 0 & 0 & 0 & 20 \end{bmatrix}^{-1} \\ &\quad \times \begin{bmatrix} 1 & 1/3 & 1/5 & 1/7 \\ 0 & 2/3 & 4/15 & 6/35 \\ 0 & 0 & 8/15 & 8/35 \\ 0 & 0 & 0 & 16/35 \end{bmatrix}^{-1} \begin{bmatrix} 92\,303\,820 \\ -503\,053\,740 \\ 55\,9142\,325 \\ 31\,974\,390 \end{bmatrix} \\ &= \frac{\pi}{1\,073\,741\,824} \begin{bmatrix} 63\,907\,767 \\ 84\,865\,536 \\ 202\,367\,970 \\ 3\,197\,439 \end{bmatrix}. \end{aligned}$$

These amplitude sets, presented in figure 7, hint at the benefits of the Zernike basis. In summary the coordinate transformation from the measurement vector c to the data vector α are

$$(4.30) \quad \begin{array}{ccccc} \begin{bmatrix} c_0 \\ \vdots \\ c_d \end{bmatrix} & \rightarrow & [T]_Y^{-1} & \rightarrow & \begin{bmatrix} a_0 \\ \vdots \\ a_d \end{bmatrix} & \rightarrow & [T]_Z^{-1} & \rightarrow & \begin{bmatrix} \alpha_0 \\ \vdots \\ \alpha_d \end{bmatrix} \\ \Upsilon(b) & & & & Y(b), \psi(r) & & & & \psi(r) \end{array}$$

Figure 7 compares the amplitudes for the input function and the response function. The points are joined to emphasize the behavior of the different vectors. Start with the approximated response function $\Upsilon(b)$ which is characterized by the amplitudes c in (4.20). Using an affine transformation like the one shown in (??) this c vector provides the amplitudes a which characterize the response function $Y(b)$ as seen in (4.4). These amplitudes represent the exact same amplitudes in $\psi(r)$ in (3.6); the modes have imprinted upon the response function. Using another affine transformation like (4.27) we transform from the monomial representation using the a coordinates to the Zernike representation in (3.5) using the α coordinates. We measure the vector c (black), transform to a (blue) and then transform to α (red). The input intensity function $\psi(r)$ is the top hat, a C^0 function, the response $Y(b)$ is a C^1 function. This causes the monomial amplitudes to begin unbounded oscillations as seen in tables (1) and (3). The orthogonal nature of the Zernike bases stabilizes these oscillations.

4.2. Extended detectors (Discrete case). Analysis is based upon a domain mapped to a quarter capsule

$$(4.31) \quad \Omega = \left\{ \begin{array}{l} \{(r, \theta) \in \mathbb{R}^2 : 0 \leq r \leq 1, 0 \leq \theta \leq \pi/4\}, \\ \{(x, y) \in \mathbb{R}^2 : 0 \leq x \leq 1, 0 \leq y \leq 1, x^2 + y^2 \leq 1\}, \end{array} \right.$$

4.2.1. Partition. The detectors with their concomitant imaging system establish a specific partition for the capsule. The detectors are idealized as having uniform

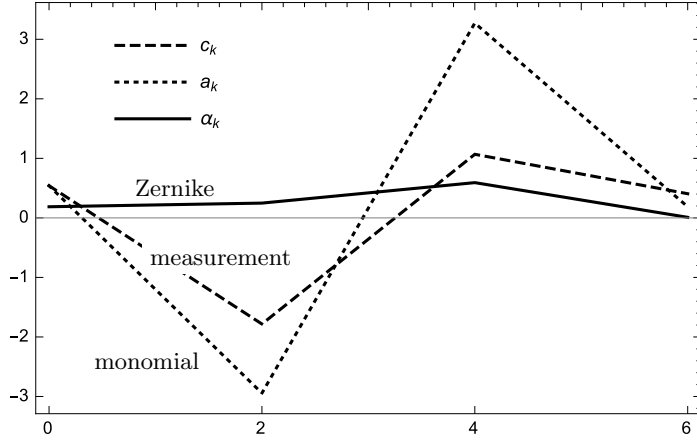
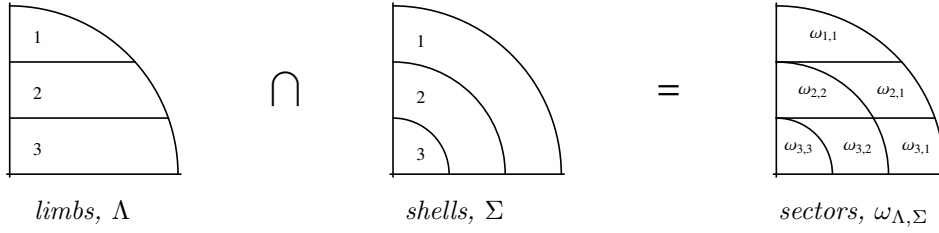


FIG. 7. The amplitudes from the validation exercise in (??).

FIG. 8. Sectors are created by the intersection of the horizontal partition (limbs) and the radial partition (shells). The numbering of the sectors $\omega_{\Lambda, \Sigma}$ is indexed to the location (limb, shell) in the capsule.

size and as providing continuous linear coverage with no overlap. This induces a horizontal partitioning as well as a radial partitioning. The intersection of these partitions defines the sectors. The collection of sectors ω covers the domain

$$(4.32) \quad \Omega = \bigcup_{k=1}^N \omega_{s_k},$$

where the number of sector N and the indexing will be defined presently. The sectors do not overlap

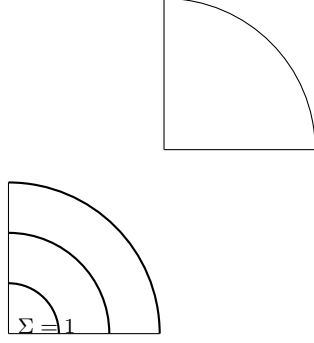
$$(4.33) \quad \omega_{s_j} \cap \omega_{s_k} = \emptyset \quad j \neq k.$$

The horizontal partition produces limbs indexed with an integer Λ and radial partition produces shells indexed with an integer Σ . A sample partition for $n = 3$ detectors is shown in figure (8).

Given n detectors the number of sectors is given by

$$(4.34) \quad N = \frac{1}{2}n(n+1)$$

This shows that the number of samples grows quadratically as the number of detectors increases.



The sector is referenced by location within a limb and within a shell.

$$(4.35) \quad \begin{aligned} s = (limb, shell) &= \{(\Lambda, \Sigma) \in \mathbb{N}^2 : \Lambda = 1, 2, \dots, n; \Sigma = 1, 2, \dots, \Lambda\} \\ &= \{(1, 1)\}, \{(2, 1), (2, 2)\}, \{(3, 1), (3, 2), (3, 3)\}, \dots \end{aligned}$$

Let $\Delta = 1/n$ represent the linear extent of a detector face. The general sector has horizontal bounds $y_1 \leq y \leq y_2$ and radial bounds $r_1^2 \leq x^2 + y^2 \leq r_2^2$. The boundary for limb Λ and shell Σ can be expressed in terms of the spacing Δ

$$(4.36) \quad y_1(\Lambda) = (\Lambda - 1)\Delta \quad r_1(\Sigma) = 1 - \Sigma\Delta,$$

$$(4.37) \quad y_2(\Lambda) = \Lambda\Delta \quad r_2(\Sigma) = 1 - (\Sigma - 1)\Delta.$$

Like peeling an onion, the first layer is on the outside.

4.2.2. Linear system. Our goal is to take the intensity measurements \mathcal{I}_k from the n detectors and compute the value of the average intensity ψ_k in each of the n shells. The capsule is represented by three zones each with a different shading. By construction the number of detectors limits the numbers of shells. A schematic system is shown in figure (9). This diagram suggests the linear system

$$(4.38) \quad \mathbf{B}\psi = \mathcal{I}$$

where the matrix \mathbf{B} encodes the contribution of each sector.

We begin with assigning the area of each sector to a corresponding matrix element in \mathbf{B} . We need to relate the indices for the limb and the shell to the row and column indices in the matrix \mathbf{B} .

$$(4.39) \quad r = \Lambda, \quad c = n - \Sigma + 1.$$

The inverse mapping is

$$(4.40) \quad \Lambda = r, \quad \Sigma = n - c + 1.$$

Partition conditions

$$(4.41) \quad \begin{aligned} y_2 - y_1 &= \Delta, \\ r_2 - r_1 &= \Delta. \end{aligned}$$

The area for the sector in limb Λ in shell Σ correlates to the \mathbf{B} matrix element in row r and column c according to

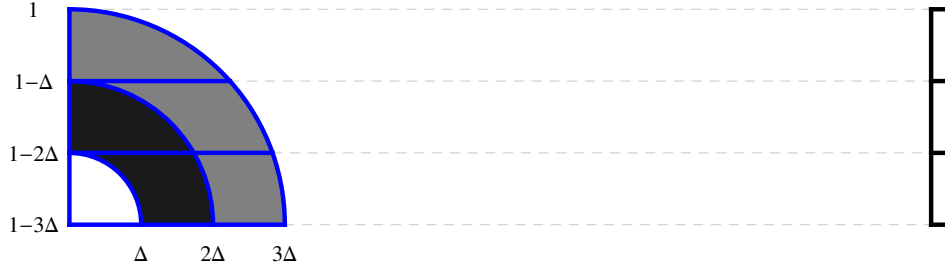


FIG. 9. The capsule, the mesh, and the detectors. The dashed lines are a visual aid to connect the detector face to the surface of the capsule.

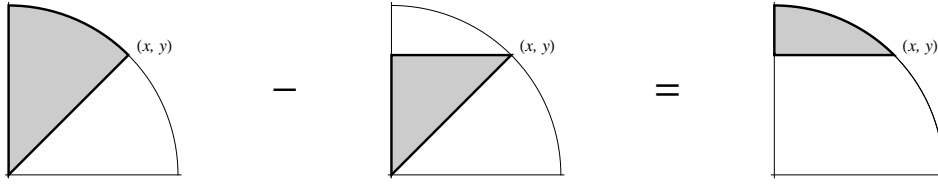


FIG. 10. Area of the upmost limb computed using geometrical methods. The result is shown in (4.42).

4.2.3. Area. Combined measurements of the limbic intensity reveal the average intensity within all sectors. To compute the intensity given the average we must compute the area for each sector. The largest sector, ω_{11} is special because the area A_{11} determines the spectral radius $\rho(\mathbf{B})$ and helps to bound the condition number. As shown in figure (10) this area follows from simple geometry.

Start with the point (x, y) on the unit circle which defines the limb-shell intersection; the area is

$$(4.42) \quad A(y) = \frac{1}{2} \left(\arccos y - y\sqrt{1-y^2} \right).$$

In terms of the mesh spacing Δ , this reference point is $(x, y) = (\sqrt{\Delta(2-\Delta)}, 1-\Delta)$ and the area becomes

$$(4.43) \quad A_{11}(\Delta) = \frac{1}{2} \left(\arccos(1-\Delta) - (1-\Delta)\sqrt{\Delta(2-\Delta)} \right).$$

For the remaining sectors we find the area of a lamina and there are three different types of surface integrals as seen in table (4). They are based on the following primitive function

$$(4.44) \quad \mathcal{A}(r, y) = \int \sqrt{r^2 - y^2} dy = \frac{1}{2} \left(r^2 \arcsin\left(\frac{y}{r}\right) + y\sqrt{r^2 - y^2} \right),$$

which generalizes (4.42) for arbitrary radius, i.e. $A(y) = \mathcal{A}(1, y)$.

TABLE 4

Three types of surface integrals are determined by boundary conditions.

type	r_1	y_1
I	$r_1 > 0$	$y_1 > 0$
II	$r_1 = 0$	$y_1 > 0$
III	$r_1 = 0$	$y_1 = 0$

The first, and most common, type of surface integral is

$$\begin{aligned}
 A^{(I)} &= \int_{y_1}^{y_2} \int_{\sqrt{r_1^2 - y^2}}^{\sqrt{r_2^2 - y^2}} dx dy = (\mathcal{A}(r_2, y) - \mathcal{A}(r_1, y)) \Big|_{y_1}^{y_2} \\
 &= \frac{1}{2} \left(y_1 \left(\sqrt{r_1^2 - y_1^2} - \sqrt{r_2^2 - y_1^2} \right) + y_2 \left(\sqrt{r_2^2 - y_2^2} - \sqrt{r_1^2 - y_2^2} \right) \right. \\
 &\quad + r_2^2 \left(\arcsin \left(\frac{y_2}{r_2} \right) - \arcsin \left(\frac{y_1}{r_2} \right) \right) \\
 &\quad \left. + r_1^2 \left(\arcsin \left(\frac{y_1}{r_1} \right) - \arcsin \left(\frac{y_2}{r_1} \right) \right) \right).
 \end{aligned}
 \tag{4.45}$$

The superscript (I) designates the most general and most common integral where $y_1 \neq 0$ and $r_1 \neq 0$.

The next type is defined by the restriction $r_1 = 0$ and $y_1 \neq 0$:

$$\begin{aligned}
 A^{(II)} &= \int_{y_1}^{y_2} \int_0^{\sqrt{r_2^2 - y^2}} dx dy = \Re \left(\int_{y_1}^{y_2} \int_{\sqrt{r_1^2 - y^2}}^{\sqrt{r_2^2 - y^2}} dx dy \right) \\
 &= \frac{1}{2} \left(y_2 \sqrt{r_2^2 - y_2^2} - y_1 \sqrt{r_2^2 - y_1^2} + r_2^2 \left(\frac{\pi}{2} - \arcsin \left(\frac{y_2}{r_2} \right) \right) \right).
 \end{aligned}
 \tag{4.46}$$

The final type is defined by the restrictions $r_1 = 0$ and $y_1 = 0$ and is

$$A^{(III)} = \int_0^\Delta \int_0^{\sqrt{\Delta^2 - y^2}} dx dy = \frac{\pi}{4} \Delta^2.
 \tag{4.47}$$

4.2.4. Dominance hierarchies. We are able to make powerful statements about the ordering of these sector areas which will be exploiting in characterizing the linear system. The two hierarchies are shown in figure (11). In part (a) the areas are ordered on a direct line of site from the outer boundary to the center. In part (b) the areas are ordered along the outer shell. Contributions from outer shell dominate the measurement; these sector areas will define the eigenvalues of our impending linear system

Diagonal dominance $a_{kk} > a_{k+1,k+1}$; dominance of column $a_{k,1} > a_{k+1,1}$

THEOREM 4 (Diagonal dominance theorem). *Given a unit disk partitioned into $n \geq 2$ shells and limbs, and two integer k such that $1 \leq k < j \leq n$.*

$$A_{kk} > A_{jj}
 \tag{4.48}$$

Proof. Employ a Matryoshka doll strategy by nesting the areas as shown in figure (12). The equation for curve $y_k(x)$ is

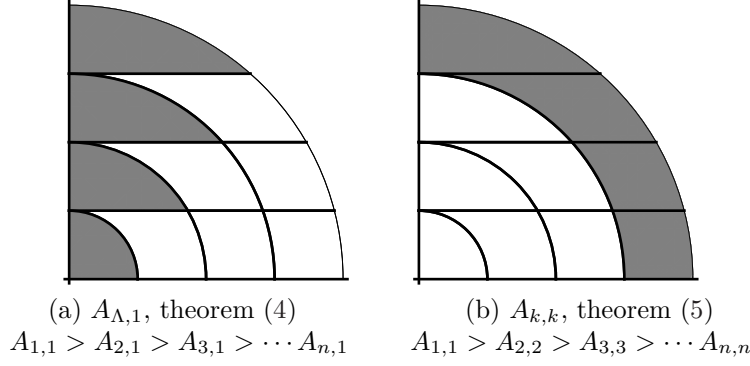


FIG. 11. Two dominance schemes will help to quantify the behavior of the system matrix \mathbf{B} to be introduced in section (4.2.6).

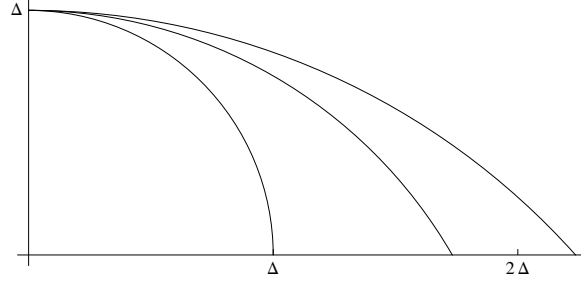


FIG. 12. Nesting the areas of interest. This is the family of curves in (4.49) for $k = 1, 2, 3$.

$$(4.49) \quad y_k(x) = \sqrt{(k\Delta)^2 - x^2} - (k-1)\Delta, \quad 0 \leq x \leq \sqrt{2k-1}\Delta.$$

Over this domain the curve $y \geq 0$. For the proof it is sufficient to show dominance over the shared domain. Given integers j and k such that $1 \leq j < k \leq n$ one must prove that

$$(4.50) \quad y_k(x) \geq y_j(x), \quad 0 \leq x \leq \sqrt{2k-1}\Delta.$$

Subtracting the Maclauren expansions leads to

$$(4.51) \quad y_k(x) - y_j(x) = \sum_{m=1}^{\infty} \binom{1/2}{m} \frac{x^{2m}}{\Delta^{2m-1}} \left(\frac{1}{j^{2m-1}} - \frac{1}{k^{2m-1}} \right).$$

By postulation, $j > k$ and each of these terms is shell positive which establishes (4.50).

□

The next theorem establishes the area ordering of the sectors on the outer shell which orders the eigenvalues and provides a reasonable approximation for the condition number.

THEOREM 5 (Dominance of the sector areas in the outer shell). *Given a unit disk partitioned into $n \geq 2$ shells and limbs, the sectors of the outer shell are ordered according to*

$$(4.52) \quad A_{11} > A_{21} > \dots > A_{n1}.$$

Proof. The proof is broken into two parts. The first is to establish the special case $A_{11} > A_{21}$ then to establish the $A_{k,1} > A_{k+1,1}$ for $2 \leq k \leq n-1$.

Part I $A_{11} > A_{21}$: Call upon equations (4.43) and (4.45) (with $y_1 = 1 - 2\Delta$ and $y_2 = 1 - \Delta$; $r_1 = 1 - \Delta$ and $r_2 = 1$):

$$(4.53) \quad (1 - \Delta)^2 \left(\arcsin \left(\frac{1 - 2\Delta}{1 - \Delta} \right) - \frac{\pi}{2} \right) + \arccos(1 - \Delta) - \arcsin(1 - \Delta) \\ + \arcsin(1 - 2\Delta) > (1 - 2\Delta) \left(\sqrt{\Delta(2 - 3\Delta)} - 2\sqrt{\Delta(1 - \Delta)} \right)$$

The right-hand side is negative for $0 < \Delta < \frac{1}{2}$ so it will suffice to show that the left hand side, $f(\Delta)$, is positive over the same domain. A Maclauren expansion produces a lead term of

$$(4.54) \quad f(\Delta) = \left(\frac{3}{\sqrt{2}} - 1 \right) \sqrt{\Delta} + \mathcal{O}(\Delta^{3/2}).$$

Near the origin this function behaves as the square root, increasing from 0 at the origin. To resolve the behavior of the function away from the origin examine the derivative

$$(4.55) \quad f'(\Delta) = \frac{2}{\sqrt{\Delta(2 - \Delta)}} + \frac{1 - \Delta}{\sqrt{\Delta(2 - 3\Delta)}} - \frac{1}{\sqrt{\Delta(1 - \Delta)}} - 2(1 - \Delta) \arccos \left(\frac{1 - 2\Delta}{1 - \Delta} \right)$$

which is positive until $\Delta \approx 0.41$ at which point it becomes negative. The function value at the boundary point is

$$(4.56) \quad f\left(\frac{1}{2}\right) = \frac{7\pi}{24} > 0.$$

Thus $f(\Delta) > 0$ on the domain $\Delta \in (0, 1/2]$.

Part II $A_{k,1} > A_{k+1,1}$: Exploit the monotonicity of the sector width using a common partition for the Riemann integral.

Let $P = \{x_0, x_1, \dots, x_\mu\}$ be a partition of the interval $[0, \Lambda]$ such that

$$(4.57) \quad 0 = x_0 < x_1 < \dots < x_{\mu-1} < x_\mu = \Lambda$$

with $\mu \geq 2$. Define the sector width as

$$(4.58) \quad w(y) = \sqrt{1 - y^2} - \sqrt{(1 - \Delta)^2 - y^2}, \quad 0 \leq y \leq 1 - \Lambda.$$

Inspection of the derivative

$$(4.59) \quad w'(y) = \frac{y}{\sqrt{(1 - \Delta)^2 - y^2}} - \frac{y}{\sqrt{1 - y^2}}$$

establishes that $w(y)$ increases monotonically on the domain $0 \leq y \leq 1 - \Lambda$.

Define the subdomain of the sectors (why?) as

$$(4.60) \quad y_\Lambda = \{y \in \mathbb{R} : (n - \Lambda)\Delta \leq y \leq (n - \Lambda + 1)\Delta\}.$$

Let t_k be a point in the subinterval $[x_{k-1}, x_k]$. The Riemann sum over the subdomain $\omega_{\Lambda,1}$ is

$$(4.61) \quad S_{\Lambda}(P, w) = \sum_{k=1}^{\mu} w((n - \Lambda)\Delta + t_k) (x_k - x_{k-1})$$

We will show $S_{\Lambda}(P, w) > S_{\Lambda+1}(P, w)$.

Define the numbers

$$(4.62) \quad \begin{aligned} M_{\Lambda,k}(P, w) &= \sup \{w((n - \Lambda)\Delta + x) : x \in [x_{k-1}, x_k]\}, \\ m_{\Lambda,k}(P, w) &= \inf \{w((n - \Lambda)\Delta + x) : x \in [x_{k-1}, x_k]\}. \end{aligned}$$

Since $w(y)$ increases monotonically on $0 \leq y < 1 - \Delta$ these numbers attain extremal values at the subdomain boundaries:

$$(4.63) \quad \begin{aligned} M_{\Lambda,k}(P, w) &= w((n - \Lambda)\Delta + x_k), \\ m_{\Lambda,k}(P, w) &= w((n - \Lambda)\Delta + x_{k-1}). \end{aligned}$$

The upper and lower Riemann sums for the partition P are

$$(4.64) \quad \begin{aligned} U_{\Lambda}(P, w) &= \sum_{k=1}^{\mu} M_{\Lambda,k}(P, w) (x_k - x_{k-1}), \\ L_{\Lambda}(P, w) &= \sum_{k=1}^{\mu} m_{\Lambda,k}(P, w) (x_k - x_{k-1}). \end{aligned}$$

Since $w(y)$ increases monotonically we can state that for any $t_k \in [x_{k-1}, x_k]$

$$(4.65) \quad m_{\Lambda,k}(P, w) \leq w((n - \Lambda)\Delta + t_k) \leq M_{\Lambda,k}(P, w)$$

which implies

$$(4.66) \quad L_{\Lambda}(P, w) \leq S_{\Lambda}(P, w) \leq U_{\Lambda}(P, w).$$

Because the arguments are ordered

$$(4.67) \quad (n - \Lambda)\Delta + x_{k-1} > (n - \Lambda - 1)\Delta + x_k$$

the functions are ordered

$$(4.68) \quad w((n - \Lambda)\Delta + x_{k-1}) > w((n - \Lambda - 1)\Delta + x_k)$$

which implies

$$(4.69) \quad m_{\Lambda}(\omega) > M_{\Lambda+1}(\omega)$$

which implies

$$(4.70) \quad L_{\Lambda}(P, w) > U_{\Lambda+1}(P, w).$$

Call $\mathcal{P}[0, 1 - \Delta]$ the set of all partitions with at least two subintervals. Then we see that for any $P \in \mathcal{P}[0, 1 - \Delta]$

$$(4.71) \quad S_{\Lambda}(P, w) > S_{\Lambda+1}(P, w)$$

which confirms

$$(4.72) \quad A_{\Lambda,1} > A_{\Lambda+1,1}, \quad \Lambda = 2, \dots, n-1.$$

□

An important point comes of consideration is the area of the shells: much more material is imaged in the outer shell compared to the innermost shell. The following proof shows this dominance is linear.

THEOREM 6 (Dominance of the shell areas). *Given a unit disk partitioned into $n \geq 2$ shells, and two integers k such that $1 \leq k, j \leq n$. The ratio of the shell areas is*

$$(4.73) \quad \zeta = \frac{2k-1}{2j-1}.$$

Proof. This is an immediate consequence from the area of shell Σ within the quarter disk:

$$(4.74) \quad A_{\Sigma} = \frac{\pi}{4} \left((\Sigma\Delta)^2 - ((\Sigma-1)\Delta)^2 \right)$$

□

4.2.5. B matrix solution. We introduce the system matrix \mathbf{B} , the crucial tool in translating limbic measurements of the average intensity \mathcal{I}_{Λ} into radial values of the specific intensity $\psi(r)$. The matrix elements b_{rc} of \mathbf{B} are the sector areas $A_{\Lambda, \text{Sigma}}$. For example,

$$(4.75) \quad \begin{bmatrix} A_{11} & 0 & 0 \\ A_{22} & A_{21} & 0 \\ A_{33} & A_{32} & A_{31} \end{bmatrix} \longrightarrow \begin{bmatrix} b_{11} & 0 & 0 \\ b_{21} & b_{22} & 0 \\ b_{31} & b_{32} & b_{33} \end{bmatrix}.$$

Formally the element in row r and column c of the system matrix \mathbf{B} is given by

$$(4.76) \quad b_{rc} = \Delta^{-2} \int_{n-\Lambda+1}^{n-\Lambda} \int_{\sqrt{(\Sigma-1)^2-y^2}}^{\sqrt{\Sigma^2-y^2}} dx dy = \Delta^{-2} \int_{n-r+1}^{n-r} \int_{\sqrt{(n-c)^2-y^2}}^{\sqrt{(n-c+1)^2-y^2}} dx dy.$$

Maps in (4.39) and (4.40) connect the two indexing schemes.

The measurements \mathcal{I}_{Λ} are made through each limb Λ and the data reduction produces the mean intensity I_{Σ} in each shell Σ . The system matrix accounts for the sector partitioning and unravels the mixing of limbs and shells. For $n = 3$ we have

$$(4.77) \quad \begin{bmatrix} b_{11} & 0 & 0 \\ b_{21} & b_{22} & 0 \\ b_{31} & b_{32} & b_{33} \end{bmatrix} \begin{bmatrix} \psi_{\Sigma=1} \\ \psi_{\Sigma=2} \\ \psi_{\Sigma=3} \end{bmatrix} = \begin{bmatrix} \mathcal{I}_{\Lambda=1} \\ \mathcal{I}_{\Lambda=2} \\ \mathcal{I}_{\Lambda=3} \end{bmatrix}$$

The result is the mean value of the specific intensity in shell Σ of the quarter disk

$$(4.78) \quad I_{\Sigma} = \frac{4\psi_{\Sigma}}{\pi \left((\Sigma\Delta)^2 - ((\Sigma-1)\Delta)^2 \right)} = \frac{4}{\pi (2\Sigma-1) \Delta^2} \psi_{\Sigma}$$

It is this mean value I_{Σ} which approximates specific intensity $I(r)$ in the transport equation (2.1). To emphasize this result refer to figure (??) which shows a function $I(r)$ plotted against the measurements I_{Σ} for a sample cases with partitions of $n = 3$ and $n = 30$.

The linear system in (4.2.5) is solved by forward substitution:

$$(4.79) \quad \psi_{\Sigma} = b_{\Sigma\Sigma}^{-1} \left(\mathcal{I}_{\Sigma} - \sum_{k=1}^{\Sigma-1} b_{\Sigma k} \psi_k \right)$$

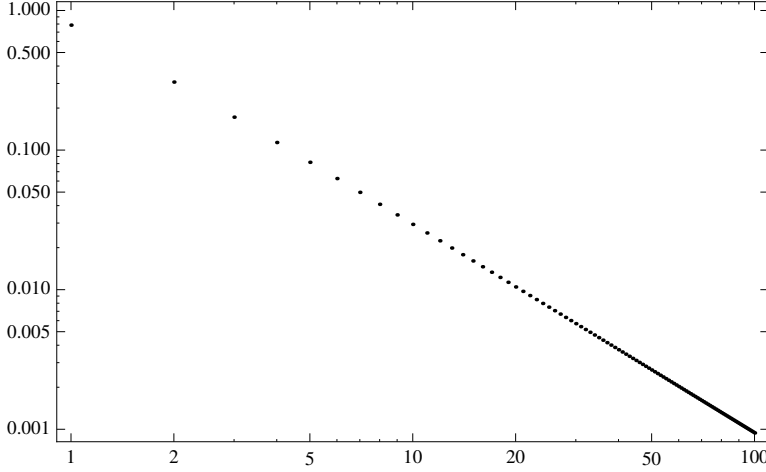


FIG. 13. *Spectral radius as a function of n for the system matrix \mathbf{B} as given in (4.81). The maximum value is $\rho(1) = \pi/4 \approx 0.785$; the decay is quadratic.*

4.2.6. \mathbf{B} matrix properties. The structure of the \mathbf{B} matrix creates a wealth of useful properties for the eigenvalues and dominance hierarchies.

As the \mathbf{B} matrix is lower triangular, the eigenvalues are displayed upon the diagonal. This connects the eigenvalue spectrum to the sector areas in the outer shell:

$$(4.80) \quad \lambda(\mathbf{B}) = \{A_{1,1}, A_{2,1}, \dots, A_{n,1}\}$$

The spectral radius is an immediate consequence.

THEOREM 4.1 (Spectral radius). *The spectral radius of the matrix \mathbf{B} with a partition of n is*

$$(4.81) \quad \rho(\mathbf{B}) = \lambda_1 = \frac{1}{2} \left(\arccos \left(\frac{n-1}{n} \right) - \frac{n-1}{n^2} \sqrt{2n-1} \right).$$

Proof. From dominance theorem (??) we see that $b_{11} = \lambda_1$ is the largest eigenvalue. To secure the above expression, take (4.43) and substitute $\Delta = 1/n$. \square

The continuum limit of the spectral radius is

$$(4.82) \quad \liminf \{\rho(\mathbf{B}) : 1 \leq n < \infty\} = 0$$

with decay $\mathcal{O}(n^{-3/2})$.

The smallest eigenvalue is

THEOREM 4.2 (Smallest eigenvalue). *In the limit $n \rightarrow \infty$, the smallest eigenvalue approaches 0 quadratically is*

$$\lim_{n \rightarrow \infty} \lambda_n = n^{-2}.$$

Proof. As the \mathbf{B} matrix is lower triangular, the eigenvalues are on the diagonal. By the diagonal dominance theorem in 4, the value of the smallest eigenvalue corresponds

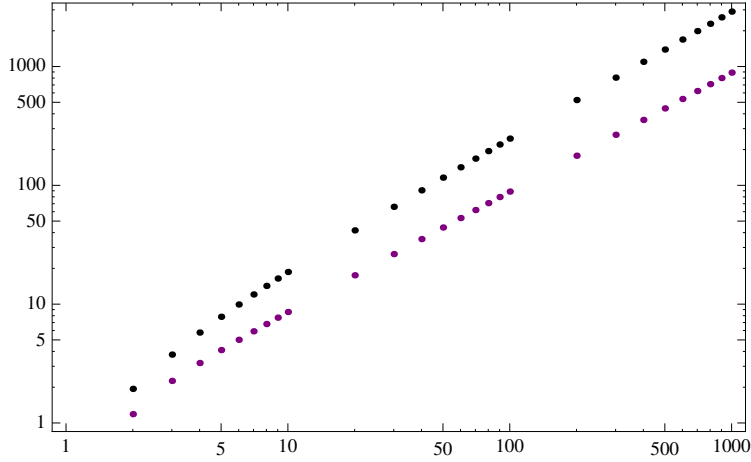


FIG. 14. The L_2 condition number (top) and the approximation using eigenvalues (bottom) for the matrix \mathbf{B} in (4.76). The system is well-conditioned, even for an extremely large number of detectors.

TABLE 5

Sector parameters in Δ coordinates for the example where $n = 3$. The scaling is related to the unit disk mapping the capsule. In this instance $3\Delta = 1$. We must satisfy the partition conditions $y_2 - y_1 = \Delta$ and $r_2 - r_1 = \Delta$.

Λ	β	r	c	y_1	y_2	r_1	r_2	integral
limb	band	\mathbf{B} row	\mathbf{B} col	lower	upper	inner	outer	type
1	1	1	1	2Δ	3Δ	2Δ	3Δ	II
2	1	2	2	Δ	2Δ	2Δ	3Δ	I
2	2	2	1	Δ	2Δ	Δ	2Δ	II
3	1	3	3	0	Δ	2Δ	3Δ	I
3	2	3	2	0	Δ	Δ	2Δ	I
3	3	3	1	0	Δ	0	Δ	III

to b_{nn} . Refer to (4.45) using $(r_1, r_2) = (1, 1 - \Delta)$, $(y_1, y_2) = (\Delta, 0)$ and apply the limit. \square

The condition of the matrix \mathbf{B} is an important property. Given the singular value spectrum $\sigma(\mathbf{B})$ the condition number in the L^2 norm is

$$(4.83) \quad \kappa_2(\mathbf{B}) = \frac{\sigma_1}{\sigma_n}.$$

That is $[\mathbf{B}, \mathbf{B}^*] \neq 0$.

$$(4.84) \quad \kappa_2(n) = \left(\frac{\sigma_{11}}{\sigma_{nn}} \right)^2 = \left(\frac{a_{11}}{a_{nn}} \right)^2$$

$$(4.85) \quad \left(\frac{\lambda_1}{\lambda_n} \right)^2 \lesssim \frac{\sigma_1}{\sigma_n} = \kappa_2$$

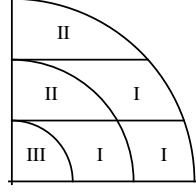


FIG. 15. Area of the upmost limb computed using geometrical methods. The result is shown in (4.45) and (4.46).

4.2.7. Example: three detectors.

$$(4.86) \quad \mathbf{A} = \begin{bmatrix} \lambda_1 & 0 & 0 \\ \frac{1}{18} \left(\frac{4\pi}{3} - \sqrt{3} \right) & \lambda_2 & 0 \\ \frac{\pi}{36} & \frac{1}{18} \left(\sqrt{3} + \frac{\pi}{6} \right) & \lambda_3 \end{bmatrix}$$

The eigenvalues $\lambda_1 > \lambda_2 > \lambda_3$ are

$$(4.87) \quad \begin{aligned} \lambda_1 &= \frac{1}{18} \left(9 \left(\frac{\pi}{2} - \arctan \left(\frac{2}{\sqrt{5}} \right) \right) - 2\sqrt{5} \right) && \approx 0.172082, \\ \lambda_2 &= \frac{1}{18} \left(-2\sqrt{2} + \sqrt{3} + 2\sqrt{5} - \frac{4\pi}{3} + 9 \left(\arctan \left(\frac{2}{\sqrt{5}} \right) - \arctan \left(\frac{1}{2\sqrt{2}} \right) \right) \right) && \approx 0.149777, \\ \lambda_3 &= \frac{1}{108} (\pi + 6\sqrt{3}) && \approx 0.125314. \end{aligned}$$

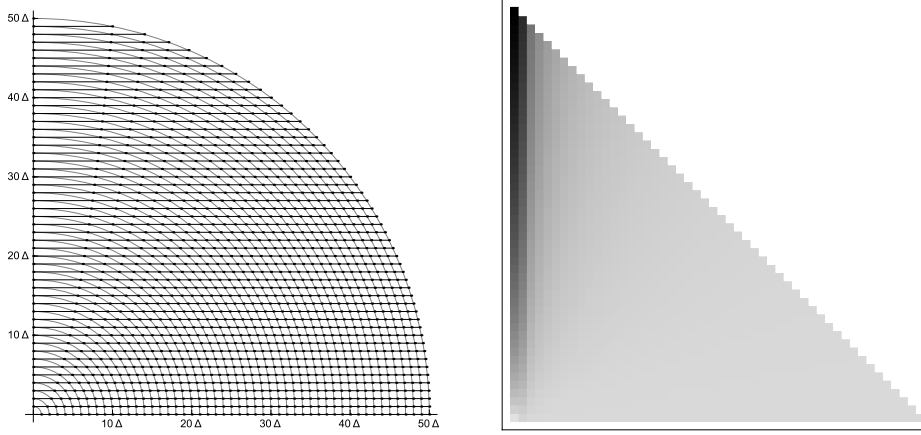
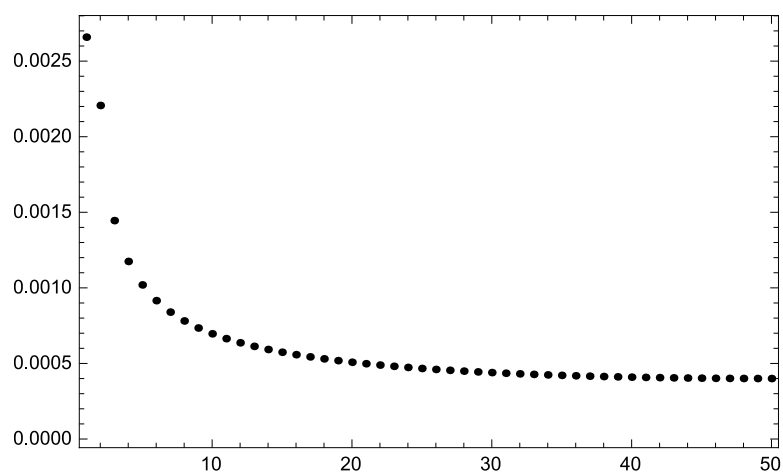


FIG. 16. A partition where $n = 50$ showing the capsule sectors (left) and the \mathbf{B} matrix (right).

4.2.8. Example: 50 detectors.

FIG. 17. *Eigenvalue spectrum.*

Appendix. Polynomials orthogonal over the unit disk. We define the \overline{D}_2 , the closed unit disk, in three different coordinate systems:

$$(A.1) \quad \overline{D}_2 = \begin{cases} \{z \in \mathbb{C}: |z| \leq 1\} \\ \{(r, \theta) \in \mathbb{R}^2: 0 \leq r \leq 1, 0 \leq \theta < 2\pi\} \\ \{(x, y) \in \mathbb{R}^2: x^2 + y^2 \leq 1\} \end{cases}$$

A.1. The set of Zernike. Given non-negative integers n for order and m for angular frequency such that $n - m$ is even. Recursion relationship: let the midpoint $\omega = \frac{1}{2}(n - m)$ and the average $\sigma = \frac{1}{2}(n + m)$ then:

$$(A.2) \quad R_n^m(r) = \sum_{j=0}^{\omega} (-1)^j \frac{(n-j)!}{j! (\omega-j)! (\sigma-j)!} r^{n-2j}$$

$$(A.3) \quad U_n^m(r, \theta) = R_n^m(r) e^{im\theta}$$

A.1.1. Change of basis. The property that makes Zernike's set dominant in practical use is the ability to use exact affine transformations to monomial sets. This allows direct connection to Seidel aberrations on an order-by-order basis and it allows exact computation of amplitudes in discrete computation where the polynomials are no longer orthogonal.

For example, two functions are equivalent almost everywhere over the unit disk

$$(A.4) \quad \begin{aligned} P_m(x_1, x_2) &= a_{00} + (a_{10}x_1 + a_{01}x_2) + (a_{20}x_1^2 + a_{11}x_1x_2 + a_{02}x_2^2), \\ P_Z(x_1, x_2) &= \alpha_{00} + (\alpha_{10}Z_1^1(x_1, x_2) + \alpha_{01}Z_1^{-1}(x_1, x_2)) \\ &\quad + (\alpha_{20}Z_2^0(x_1, x_2) + \alpha_{11}Z_2^2(x_1, x_2) + \alpha_{02}Z_2^{-2}(x_1, x_2)), \end{aligned}$$

$$(A.5) \quad \begin{bmatrix} \alpha_{00} \\ \alpha_{10} \\ \alpha_{01} \\ \alpha_{20} \\ \alpha_{11} \\ \alpha_{02} \end{bmatrix} = \begin{bmatrix} 1 & 0 & 0 & -1 & 0 & 0 \\ 0 & 1 & 0 & 0 & 0 & 0 \\ 0 & 0 & 1 & 0 & 0 & 0 \\ 0 & 0 & 0 & 2 & 1 & 0 \\ 0 & 0 & 0 & 0 & 0 & 2 \\ 0 & 0 & 0 & 2 & -1 & 0 \end{bmatrix}^{-1} \begin{bmatrix} a_{00} \\ a_{10} \\ a_{01} \\ a_{20} \\ a_{11} \\ a_{02} \end{bmatrix}$$

A.2. The set of Bhatia and Wolf. Appendix. Emissivity and opacity.

While the radiative transport equation is elementary the components are quite intricate. The terms j and α encode the interactions between the electrons, ions and radiation inside the capsule.

$$(B.1) \quad j(T, \rho) = a_{00} + \sum_{j=0}^d \sum_{k=0}^d a_{j-k,k} T^{j-k} \rho^k$$

Figure 10: The error is shown in parentheses next to each amplitude. For example, the $a_{00} = 0.01861 \pm 0.000055$. The residual error in the L_∞ norm is XX, in the L_2 norm XX.

TABLE 6
The lowest order Zernike polynomials in three different coordinate systems.

n	m	Complex coordinates	Polar coordinates	Cartesian coordinates
0	0	1	Re: 1 Im: 0	Re: 1 Im: 0
1	1	z	Re: $r \cos \theta$ Im: $r \sin \theta$	Re: x Im: y
2	0	$2 z ^2 - 1$	Re: $2r^2 - 1$ Im: 0	Re: $2(x^2 + y^2) - 1$ Im: 0
2	2	z^2	Re: $r^2 \cos 2\theta$ Im: $r^2 \sin 2\theta$	Re: $(x - y)(x + y)$ Im: $2xy$
3	1	$z(3 z ^2 - 2)$	Re: $(3r^2 - 2r) \cos \theta$ Im: $(3r^2 - 2r) \sin \theta$	Re: $x(3(x^2 + y^2) - 2)$ Im: $y(3(x^2 + y^2) - 2)$
3	3	z^3	Re: $r^3 \cos 3\theta$ Im: $r^3 \sin 3\theta$	Re: $x^3 - 3xy^2$ Im: $-y^3 + 3yx^2$
4	0	$6 z ^4 - 6 z ^2 + 1$	Re: $6r^4 - 6r^2 + 1$ Im: 0	Re: $6(x^2 + y^2)^2 - 6(x^2 + y^2) + 1$ Im: 0
4	2	$z^2(4 z ^2 - 3)$	Re: $(4r^4 - 3r^2) \cos 2\theta$ Im: $(4r^4 - 3r^2) \sin 2\theta$	Re: $(x - y)(x + y)(4(x^2 + y^2) - 3)$ Im: $2xy(4(x^2 + y^2) - 3)$
4	4	z^4	Re: $r^4 \cos 4\theta$ Im: $r^4 \sin 4\theta$	Re: $x^4 + y^4 - 6x^2y^2$ Im: $2xy(x - y)(x + y)$
5	1	$z(10 z ^4 - 12 z ^2 + 3)$	Re: $(3r^2 - 2r) \cos \theta$ Im: $(3r^2 - 2r) \sin \theta$	Re: $x(10x^4 + 4x^2(5y^2 - 3) + 10y^4 - 12y^2 + 3)$ Im: $y(10x^4 + 4x^2(5y^2 - 3) + 10y^4 - 12y^2 + 3)$
5	3	$z^3(5 z ^2 - 4)$	Re: $(5r^5 - 4r^3) \cos 3\theta$ Im: $(5r^5 - 4r^3) \sin 3\theta$	Re: $5x^5 - 10x^3y^2 - 15xy^4 - 4x^3 + 12xy^2$ Im: $-5y^5 + 10y^3x^2 + 15yx^4 + 4y^3 - 12yx^2$
5	5	z^5	Re: $r^5 \cos 5\theta$ Im: $r^5 \sin 5\theta$	Re: $x^5 - 10x^3y^2 + 5xy^4$ Im: $y^5 - 10y^3x^2 + 5yx^4$
6	0	$20 z ^6 - 30 z ^4 + 12 z ^2 - 1$	Re: $20r^6 - 30r^4 + 12r^2 - 1$ Im: 0	Re: $(2x^2 + 2y^2 - 1)(10((x - 1)x + y^2)(x^2 + x + y^2) - 10y^2 + 1)$ Im: 0
6	2	$z^2(15 z ^4 - 20 z ^2 + 6)$	Re: $r^2(15r^4 - 20r^2 + 6) \cos 3\theta$ Im: $r^2(15r^4 - 20r^2 + 6) \sin 3\theta$	Re: $(x - y)(x + y)(15(x^4 + y^4) - 20(x^2 + y^2) + 30x^2y^2 - 6)$ Im: $2xy(15(x^4 + y^4) - 20(x^2 + y^2) + 30x^2y^2 - 6)$
6	4	$z^4(6 z ^2 - 5)$	Re: $r^4(6r^2 - 5) \cos 4\theta$ Im: $r^4(6r^2 - 5) \sin 4\theta$	Re: $(x^2 - 2xy - y^2)(x^2 + 2xy - y^2)(6x^2 + 6y^2 - 5)$ Im: $4xy(x - y)(x + y)(6x^2 + 6y^2 - 5)$
6	6	z^6	Re: $r^6 \cos 6\theta$ Im: $r^6 \sin 6\theta$	Re: $(x - y)(x + y)(x^4 - 14x^2y^2 + y^4)$ Im: $2xy(3x^4 - 10x^2y^2 + 3y^4)$

TABLE 7

The emissivity j as a function of density and temperature plotted with a common color scale.

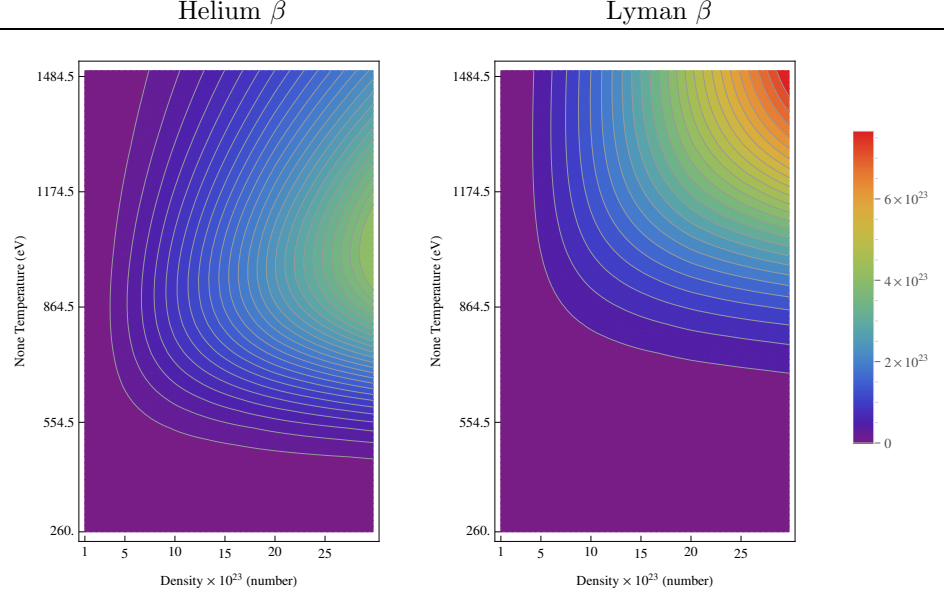


TABLE 8

The opacity α as a function of density and temperature plotted with a common color scale.

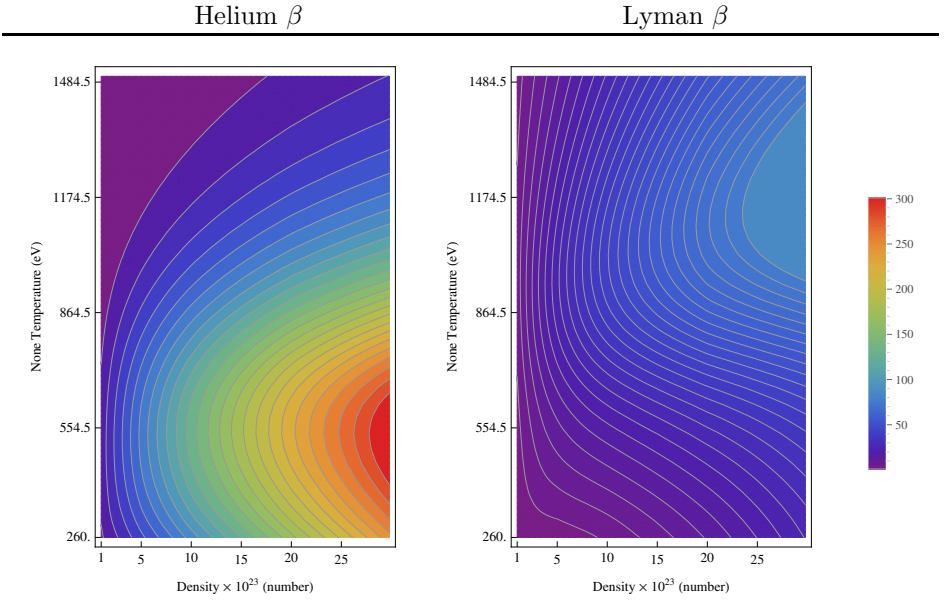


TABLE 9

Quality measures for the surface fit as a function of maximum fit order. There are three different kinds of metrics shown here. The first is the matrix condition number. The next two are norms: the first is L_2 , the second L_∞ .

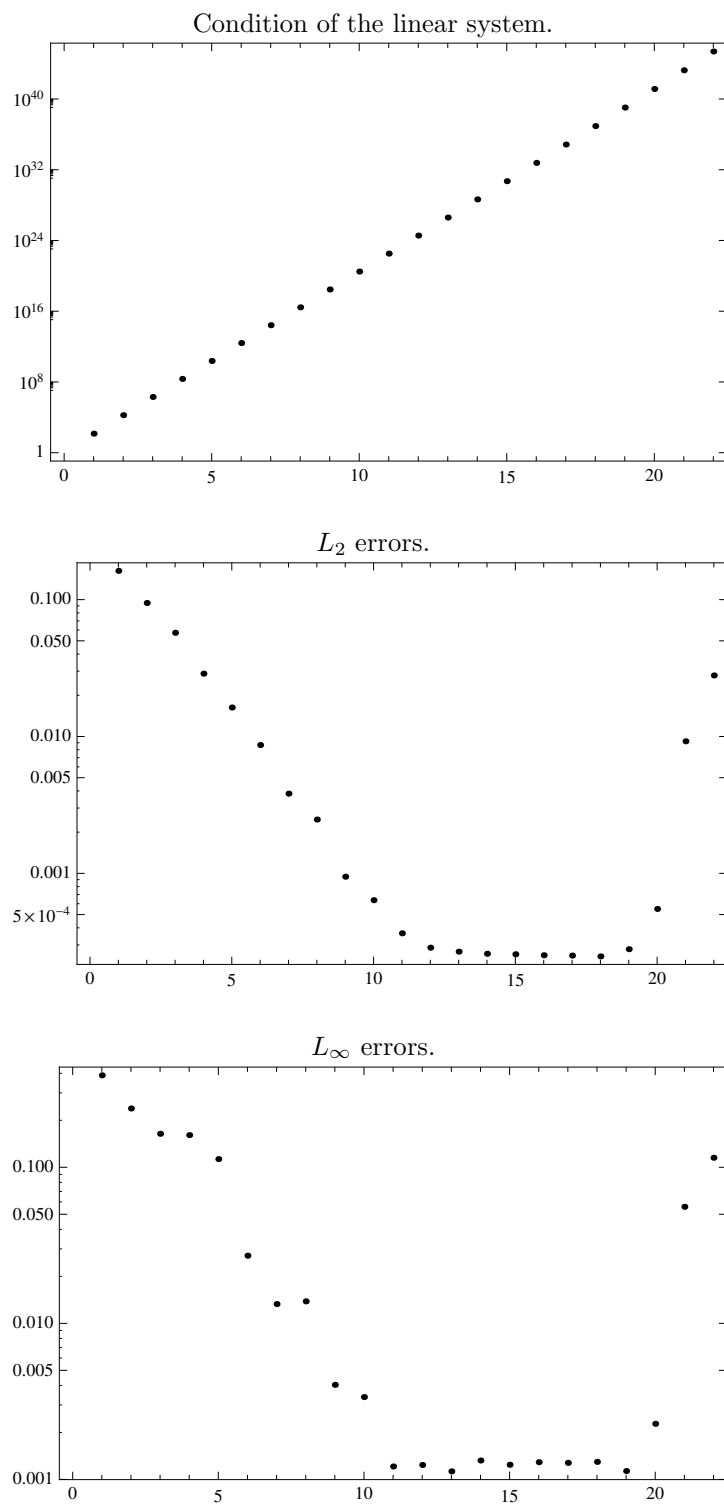


TABLE 10

Surface fit amplitudes with errors for the normalized opacity α of the He β line for orders 0 – 10.

k	i	j	$x^i y^j$	a_{ij}		k	i	j	$x^i y^j$	a_{ij}	
1	0	0	1	1.861 (55)	E – 02	37	8	0	x^8	2.452 (34)	E – 12
						38	7	1	$x^7 y$	4.85 (40)	E – 13
2	1	0	x	–5.8 (20)	E – 04	39	6	2	$x^6 y^2$	1.113 (55)	E – 12
3	0	1	y	1.349 (36)	E – 02	40	5	3	$x^5 y^3$	–1.126 (82)	E – 12
						41	4	4	$x^4 y^4$	3.6 (13)	E – 13
4	2	0	x^2	7.06 (37)	E – 04	42	3	5	$x^3 y^5$	0.5 (21)	E – 13
5	1	1	xy	1.746 (48)	E – 03	43	2	6	$x^2 y^6$	1.20 (36)	E – 12
6	0	2	y^2	2.3 (11)	E – 04	44	1	7	xy^7	–9.3 (67)	E – 13
						45	0	8	y^8	2.36 (15)	E – 11
7	3	0	x^3	–1.219 (38)	E – 04						
8	2	1	$x^2 y$	–7.00 (45)	E – 05	46	9	0	x^9	–1.442 (19)	E – 14
9	1	2	xy^2	–5.78 (73)	E – 05	47	8	1	$x^8 y$	6.1 (24)	E – 16
10	0	3	y^3	–5.8 (17)	E – 05	48	7	2	$x^7 y^2$	–1.087 (34)	E – 14
						49	6	3	$x^6 y^3$	8.09 (50)	E – 15
11	4	0	x^4	9.93 (23)	E – 06	50	5	4	$x^5 y^4$	1.32 (77)	E – 15
12	3	1	$x^3 y$	3.62 (26)	E – 06	51	4	5	$x^4 y^5$	–4.8 (12)	E – 15
13	2	2	$x^2 y^2$	2.15 (39)	E – 06	52	3	6	$x^3 y^6$	3.8 (20)	E – 15
14	1	3	xy^3	2.8 (68)	E – 07	53	2	7	$x^2 y^7$	–1.93 (35)	E – 14
15	0	4	y^4	1.03 (16)	E – 05	54	1	8	xy^8	1.22 (63)	E – 14
						55	0	9	y^9	–2.21 (13)	E – 13
16	5	0	x^5	–4.627 (87)	E – 07						
17	4	1	$x^4 y$	–2.324 (97)	E – 07	56	10	0	x^{10}	3.599 (46)	E – 17
18	3	2	$x^3 y^2$	2.2 (14)	E – 08	57	9	1	$x^9 y$	–1.025 (63)	E – 17
19	2	3	$x^2 y^3$	–7.6 (23)	E – 08	58	8	2	$x^8 y^2$	3.631 (97)	E – 17
20	1	4	xy^4	5.4 (41)	E – 08	59	7	3	$x^7 y^3$	–1.82 (15)	E – 17
21	0	5	y^5	–9.28 (96)	E – 07	60	6	4	$x^6 y^4$	–1.68 (24)	E – 17
						61	5	5	$x^5 y^5$	1.59 (38)	E – 17
22	6	0	x^6	1.313 (21)	E – 08	62	4	6	$x^4 y^6$	7.2 (61)	E – 18
23	5	1	$x^5 y$	6.90 (24)	E – 09	63	3	7	$x^3 y^7$	–2.19 (98)	E – 17
24	4	2	$x^4 y^2$	–6.2 (34)	E – 10	64	2	8	$x^2 y^8$	1.12 (16)	E – 16
25	3	3	$x^3 y^3$	1.8 (53)	E – 10	65	1	9	xy^9	–7.0 (26)	E – 17
26	2	4	$x^2 y^4$	1.62 (88)	E – 09	66	0	10	y^{10}	8.75 (49)	E – 16
27	1	5	xy^5	–2.2 (16)	E – 09						
28	0	6	y^6	4.64 (37)	E – 08						
29	7	0	x^7	–2.308 (34)	E – 10						
30	6	1	$x^6 y$	–9.34 (39)	E – 11						
31	5	2	$x^5 y^2$	–3.63 (54)	E – 11						
32	4	3	$x^4 y^3$	5.30 (82)	E – 11						
33	3	4	$x^3 y^4$	–3.4 (13)	E – 11						
34	2	5	$x^2 y^5$	–3.7 (22)	E – 11						
35	1	6	xy^6	4.9 (41)	E – 11						
36	0	7	y^7	–1.365 (93)	E – 09						

REFERENCES

- [1] A. B. BHATIA, AND E. WOLF, *On the circle polynomials of Zernike and related orthogonal sets*, Math. Proc. Cambridge Phil. Soc., 50 (1954), pp. 40-48.
- [2] D. G. HUMMER, AND G. B. RYBICKI, *Radiative transfer in spherically symmetric systems. The conservative grey case*, Mon. Not. R. Astr. Soc., 152 (1971), pp. 1-19.
- [3] T. T. TRENT, *A Müntz-Szász theorem for $C(\overline{D})$* , Proc. Am. Math. Soc., 83 (1981), pp. 296-298.
- [4] D. M. TOPA, AND P. F. EMBID, *Orthogonality, domains and linear independence*, some computation journal (in print).
- [5] D. M. TOPA, AND P. F. EMBID, *Surprising homotopies in the Zernike bases*, Applied Computational and Harmonic Analysis (in print).
- [6] F. ZERNIKE, *Diffraction theory of the knife-edge test and its improved form, the phase-contrast method*, Mon. Not. R. astr. Soc., 94 (1934), 377-384.